

## Full length article

## On the origin of microstructural banding in Ti-6Al4V wire-arc based high deposition rate additive manufacturing

Alistair Ho<sup>a</sup>, Hao Zhao<sup>a</sup>, Jon W. Fellowes<sup>b</sup>, Filomeno Martina<sup>c</sup>, Alec E. Davis<sup>a</sup>, Philip B. Prangnell<sup>a,\*</sup><sup>a</sup> School of Materials, The University of Manchester, M13 9PL, UK<sup>b</sup> School of Earth and Environmental Sciences University of Manchester, M13 9PL, UK<sup>c</sup> Welding Engineering and Laser Processing Centre, Cranfield University, Bedfordshire, MK43 0AL, UK

## ARTICLE INFO

## Article history:

Received 22 October 2018

Received in revised form

19 December 2018

Accepted 20 December 2018

Available online 4 January 2019

## Keywords:

Additive manufacturing

Titanium

Microstructure

Heat affected zones

Phase transformations

## ABSTRACT

Directed energy high deposition-rate additive manufacturing processes involve a larger melt pool diameter (~5–10 mm) and layer height (1–2 mm) than powder bed technologies, which generally leads to greater microstructural heterogeneity and more severe Heat Affected Zone (HAZ) banding. While HAZ banding has been widely reported in AM, in this study the banding features seen in samples produced by Wire-Arc Additive Manufacturing (WAAM) have been more rigorously quantified than previously possible, using statistically reliable compositional and, purpose developed, microstructure analysis mapping tools, which has provided new insight into their nature and mechanisms of formation. In addition to HAZ banding, a segregation layer has also been discovered at the fusion boundary from each melt track. This transient segregation layer and the weak coring seen, for the first time in the AM deposits, can be attributed to the lower partition coefficient of Fe in titanium, as well as limited V and Al segregation. The detailed microstructure evolution occurring in the HAZ bands has been revisited, based on new evidence, and is shown to involve both dark and white etching bands. The lower temperature dark etching region is caused not just by an increase in the  $\alpha$  lamellar spacing due to coarsening, but also by greater chemical partitioning with temperature rise. In addition, it is shown by thermal simulation that the thin white band occurs on re-heating to just below the  $\beta$  transus temperature, which is shifted upwards owing to the high heating rate in AM. This white band is associated with a morphological change to a fine  $\alpha$  lamellar colony morphology, which exhibits less solute partitioning. The mechanisms involved are discussed. The rapid coarsening that occurs in the range of the  $\beta$  approach curve is attributed to interface migration from  $\beta$  re-growth, rather than conventional surface tension driven effects, whereas the fine colony microstructure is proposed to be caused by colony nucleation, in subsequent cooling, on a low volume fraction of residual  $\alpha$ .

© 2019 The Authors. Published by Elsevier Ltd on behalf of Acta Materialia Inc. This is an open access article under the CC BY license (<http://creativecommons.org/licenses/by/4.0/>).

## 1. Introduction

A range of additive manufacturing AM technologies are now available that use different heat sources' (e.g. laser, E-beam, plasma-electric arc) and material feedstocks (e.g. powder or wire), but in general there is a trade-off between the limiting part size, deposition rate, and layer height-resolution [1–7]. To economically produce large airframe parts, high deposition rates of kilograms per hour and build envelopes of several meters are required. Direct

Energy Deposition (DED) wire-fed AM processes with higher power heat sources are most suitable for such applications [3–5,7]. Currently, a number of systems are under development including; laser [8], and E-beam based (NASA, Sciaky™) [9,10] and Wire-Arc Additive Manufacturing (WAAM) (e.g. Cranfield University, Norsk Titanium [11–14]). All of these processes are similar in concept, in that they use a directed heat source and employ travel speeds of 5–15 mm s<sup>-1</sup>, with melt pool sizes in range of 2–10 mm wide, and a layer height of 1–2 mm [5–13]. This results in substantially lower solidification and cooling rates than found in powder bed systems. For example, the cooling rates in a powder bed process are typically 10<sup>4–5</sup> K s<sup>-1</sup> and in a wire DED are less than 10<sup>2</sup> K s<sup>-1</sup> [4,6,15–17]. Such scaling effects can cause greater heterogeneity and anisotropy

\* Corresponding author.

E-mail address: [philip.prangnell@manchester.ac.uk](mailto:philip.prangnell@manchester.ac.uk) (P.B. Prangnell).

in the deposited material than in powder bed processes (e.g. Refs. [4,11,18–20]), which is an important consideration when qualifying aerospace parts.

The alpha ( $\alpha$ ) - beta ( $\beta$ ) titanium alloy Ti-6Al-4V (Ti64) is extensively used in the aerospace industry owing to its excellent combination of mechanical properties [21]. The transformation microstructures that arise in high deposition rate AM processes with Ti64 typically includes fine Widmanstätten colony and basketweave lamella- $\alpha$  morphologies with a fine  $\alpha$  plate spacing of  $\sim 0.7$ – $1.2\ \mu\text{m}$  [8,11,12,19,20,22]. In some research a partially martensitic region has also been reported near the top surface of deposition tracks [11,20,23], but the cooling rate in the bulk of a part with most wire-based high deposition rate AM processes is generally lower than  $100\ \text{K s}^{-1}$  [16,17], which is less than that required to produce martensite ( $\sim 400\ \text{K s}^{-1}$  [21,24]). An undesirable feature of AM with Ti64 is the formation of coarse-columnar primary  $\beta$ -grain structures with an associated strong solidification texture [4,5,11,18,23,25]. In DED processes the columnar  $\beta$  grains are observed to grow through multiple layers and can be centimetres in scale [5,18,25]. This coarse grain structure arises from epitaxial re-growth of  $\beta$ -grains from the fusion boundary [4,6,11,18,25] and results from the solidification conditions in a heated moving melt pool, which promote a steep positive thermal gradient at the solidification front, and the Ti64 alloy itself, which does not lend itself to nucleation ahead of the solidification front because the partition coefficients ( $k$ ) of aluminium (Al) and vanadium (V) are close to unity [25–28]. This leads to minimal constitutional undercooling and a narrow mushy zone, which also prevents nucleation by dendrite fragmentation [28]. However, the narrow freezing-range is a major advantage in AM as it results in a low tendency for solidification cracking and microsegregation. Indeed, to date no solidification-related segregation effects have been reported in Ti64 AM deposits, while inter-dendritic coring is a common with other alloy systems (e.g. nickel-based superalloys [29]). More negatively, the coarse prior  $\beta$ -grain structure and related weaker  $\alpha$  transformation texture contribute to the mechanical anisotropy of AM Ti64 [19,20,30].

In AM repeated translation of the heat source can lead to systematic microstructure variation [1,2,4–7,20] as the material is ‘affected’ by the moving thermal field from the sequential deposition passes such that, within a given added layer, each location experiences a cyclic thermal history with a diminishing peak temperature [4,6,7,20,23]. The local thermal conditions will also depend on the process variables (e.g. power, speed, wire feed rate etc.), part geometry, and raster strategy [1–7]. It has been widely reported that the thermal cycling experienced in AM can result in regularly spaced heat affected zone (HAZ) ‘bands’ being produced in deposits [8,11,19,20,31–35]. Such features are seen in etched optical cross-section images (see Fig. 1) as parallel bands in single track wide walls, or as a curved ‘fish scale’ motif where multiple passes are used for each layer. The HAZ bands are observed to have a regular spacing equivalent to the layer height, but are not found in the last layers of the as-deposited material that is fully  $\beta$  annealed by the final deposition pass [32,33]. Similar HAZ bands have been observed with all wire-based AM processes [8,11,19,20] and also in powder-based DED (e.g. Laser Metal Deposition (LMD) [31–34]) and more weakly in powder bed processes [22–24]. However, due to the greater layer height, they are more prominent in high deposition rate processes like WAAM.

HAZ banding in titanium AM was first reported by Kobryn and Semiatin [31] to be caused by re-heating of the substrate material to close to the  $\beta$  transus temperature ( $T_\beta$ ). In a more detailed subsequent study by Kelly and Kampe [32,33], on Ti6Al4V samples produced by an LMD system, the microstructure variation across each HAZ band was described in terms of coarsening of the  $\alpha$  lamellar

relative to the peak temperature reached locally in the range where the  $\alpha$  volume fraction started to reduce, as a result of the re-growth of  $\beta$ . This work has been widely cited in subsequent observations of coarsening of the transformation microstructure within HAZ bands reported by other groups (e.g. Refs. [20,34]). In their original work Kelly and Kampe [32,33] also noted a thin layer with a fine  $\alpha$  lamellar colony microstructure at the top of each HAZ band, which they associated with heating ‘just above’ the  $\beta$  transus temperature. They proposed that this microstructure, which is in competition with the basketweave morphology, was promoted by a specific combination of time at peak temperature and cooling rate. However, a colony structure is normally thought to be nucleated by  $\beta$  grain boundaries [21] and the  $\beta$  grain size is typically too large in AM to account for the presence of a continuous microstructure layer. The origins of this microstructure have thus not yet been satisfactory explained, although it is apparent in other papers (e.g. Ref. [34] Fig. 4(f)) and has also been associated with a local change in  $\alpha$  texture [19]. In addition, Kelly and Kampe [32] found no evidence of compositional banding in their LMD samples and there have been no subsequent reports of compositional variation in Ti64 deposits produced by DED, which is surprising given then difference in etching contrast. More recently it has been suggested by Zhu et al., in a Ti–6.5Al–3.5Mo–1.5Zr–0.3Si alloy, that the reduction in  $\alpha$  phase volume fraction with temperature can result in a HAZ band layer with a bimodal microstructure containing primary  $\alpha$  [34]. Baufeld et al. [8] have also noted small regions of secondary  $\alpha$  in Ti64 laser-wire HAZs. In addition, Zhu et al. have observed a second type of white-etching ‘interlayer’ thinner microstructure banding feature seen between the HAZ bands, not previously reported, that occurred near the fusion boundary for each melt track [34]. They attributed this feature to ‘chemical composition homogenization’ at high temperatures in the  $\beta$  phase.

Finally, given that AM is a solidification process and that the solidification velocities in high deposition rate AM are too low to expect significant solute trapping, it is perhaps surprising that there are no reports of any microsegregation effects in Ti64 AM deposits. In Ti64 the main alloy elements have partition coefficients close to unity [27,28], which may explain this anomaly, but trace elements present in the alloy like Fe (theoretically  $k = 0.38$  [27,28]) might be expected to show stronger partitioning during solidification.

While the heterogeneity caused by HAZ banding in Ti AM has attracted considerable interest (e.g. Refs. [8,11,20,31–34]), to date discussion of the mechanisms of the microstructure evolution within the bands has been limited in scope and largely based on qualitative observations, or limited manual measurements, and has not fully explained several of the observations noted above. To better understand the nature of HAZ banding regions found in high deposit rate AM processes, we have therefore utilised a multi-scale approach to quantify important characteristics, such as the  $\alpha$  lamellar spacing, with statistically significant data across multiple layers, as well as high resolution measurements of composition variation and texture. This has been supported by the use of thermal simulations to investigate the effect of rapid heating on the transus temperature and to replicate the thermal cycle experienced in the regions of interest. Based on these new results, we have clarified some of the earlier observations and provided a more detailed description of the mechanisms involved in formation of HAZ banding heterogeneities in titanium AM parts. As part of this work, we have also noted a second type of compositional-related banding in the WAAM deposits, which is again discussed. Although the samples studied were exclusively produced by the WAAM process, it should be noted that the conclusions are applicable to all high deposition rate AM processes and are also relevant to titanium welding.

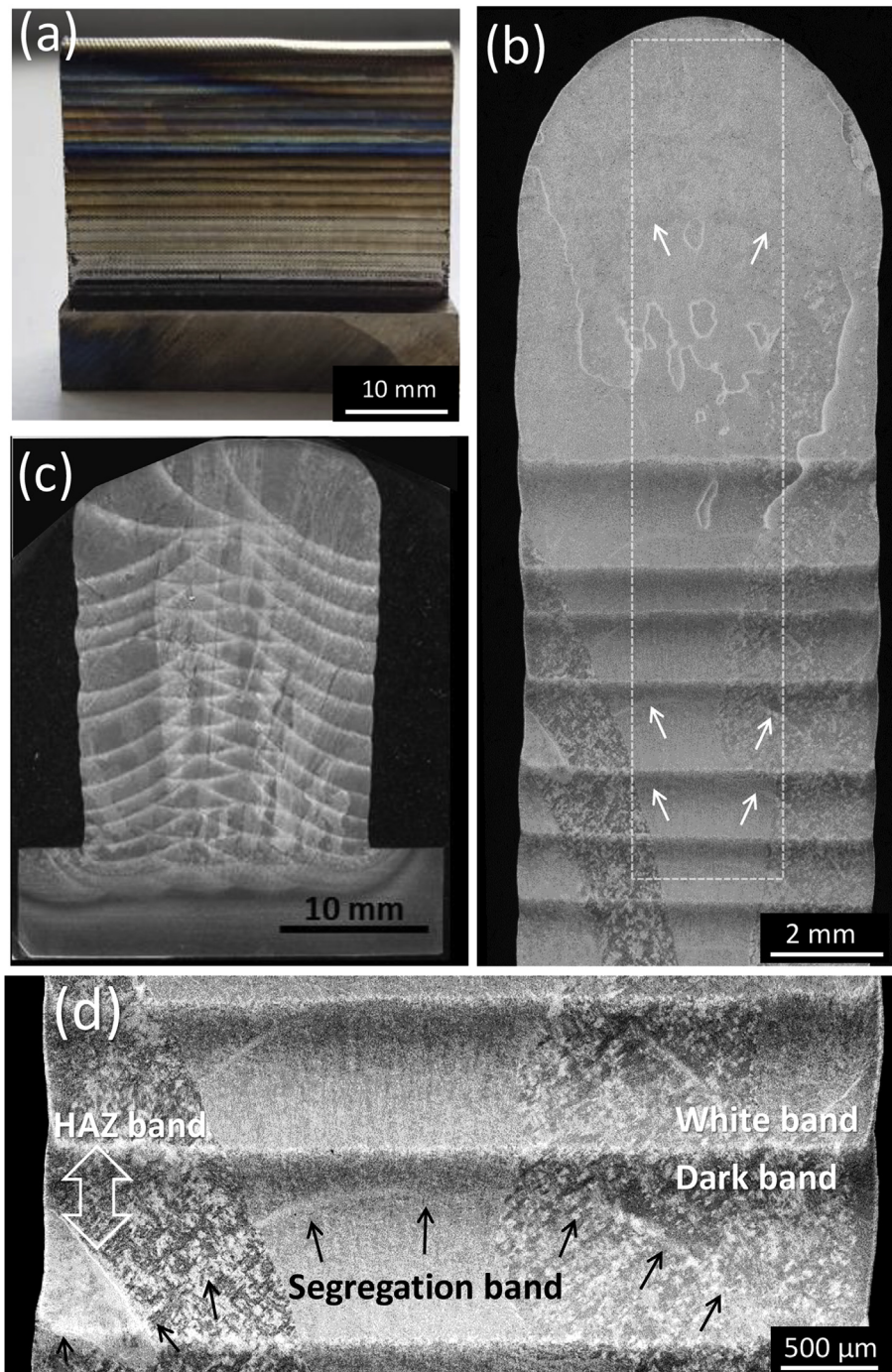


**Fig. 1.** (a) A single pass wide WAAM wall and (b) its optical cross sections; (c) a macroscopic image of a four bead wide wall after etching. In (b) parallel HAZ bands revealed by etching with Kroll's reagent are readily apparent along with a weaker thinner, curved, fusion boundary band; the typical contrast seen across each type of band in an optical microscope is highlighted in (d) at higher magnification. The dashed box in (b) indicates the position of the large area EPMA maps shown in Fig. 3.

## 2. Experimental methods

WAAM linear wall specimens were produced using a 1.2 mm diameter Ti64 wire with a Tungsten Inert Gas (TIG) torch and a local argon shielding device. The processing parameters used are shown on Table 1. Full details of the WAAM process can be found in Refs. [11,12,20]. The samples studied were built as single-bead wide walls, with a width of ~7 mm, and the heat source translated parallel to the wall length. The sample reference frame used throughout is defined as: x is the heat source travel direction

parallel to each wall (or 'welding' direction, WD), y the transverse direction (TD) and, z the build height direction normal to each layer (ND).

To measure the thermal history of the builds, R-type thermocouples were plunged manually into the melt pool (the so-called "harpoon" method). Their final position was subsequently checked by x-ray tomography so that data could be obtained from the centre of a typical melt pass. This information was subsequently used to simulate the microstructures developed across a HAZ band in a TA Instruments DIL 805A/D/T quench-dilatometer. Cubic



**Table 1**  
WAAM build parameters.

Wire feed speed	1.9 m min <sup>-1</sup>
Travel speed	4.5 mm s <sup>-1</sup>
Peak current	150 A
Background current	70 A
Average current	110 A
Pulse duration	0.5 s
Frequency	10 Hz
Gas flow rate	10 l min <sup>-1</sup>
Trailing shield gas flow rate	20 l min <sup>-1</sup>
Electrode-to-workpiece stand-off (mm) (mm)	3.5 mm

specimens 5 mm in dimension were extracted from a WAAM build for this purpose and first  $\beta$  annealed by heating above the  $\beta$  transus (to 1100 °C) and cooling with the same cooling rate of 30 K s<sup>-1</sup> recorded in the process (See below), to obtain a starting microstructure similar to that seen in the top layer of a WAAM deposit. The specimens were then re-heated with a rate of ~400 K s<sup>-1</sup> to a range of peak temperatures below and above  $T_{\beta}$  and cooled to room temperature at a cooling rate of 30 K s<sup>-1</sup>. In a second set of experiments, the dilatometer was used to measure the effect of heating rate on the  $\beta$  transus temperature by recording the shift in the inflection caused by the termination of the physical expansion from the  $\alpha_{\text{HCP}}$  to  $\beta_{\text{BCC}}$  transformation. The heating rates investigated were in the range of 0.5–630 K s<sup>-1</sup>; where the baseline of 0.5 K s<sup>-1</sup> is similar to that for a standard industrial furnace  $\beta$ -annealing treatment.

Metallographic sample preparation was performed on samples sectioned in the y-z (ND-TD) plane, using a series of abrasive grinding papers with decreasing coarseness to 4000 grit, followed by final polishing with an OPS suspension mixed with 5% concentrated hydrogen peroxide (H<sub>2</sub>O<sub>2</sub>). Optical images of the samples were obtained using a Keyence VHX-5000 microscope with the specimens etched in Kroll's reagent.

To obtain statistically-reliable quantitative microstructure data across long distances in the AM specimens, a bespoke image processing tool developed by Zhao [22,35] was employed in conjunction with the FEI MAPS software available on the Magellan FEGSEM platform. With this approach data could be mapped at high magnification, automatically, with good statistics, so that fine microstructural detail could be captured across large sample areas. A series of 100–200 by 5 wide image tile strips, with a horizontal image width of 25  $\mu\text{m}$ , were taken across pre-selected sample positions. The image tiles were obtained using the concentric backscattered detector, with the SEM operated at 8 kV with a 1.6 nA beam current and 4 mm working distance, and batch processed through the automated image analysis tool. This procedure involved pre-processing to provide 'clean' background-corrected images by combining dynamic background subtraction, via a low-pass Gaussian filter, with a median filter, to suppress noise, followed by grey-scale optimisation. Canny's edge detection method [36] was then employed to define the phase boundaries so that the  $\alpha$  inter-lamellar spacing could be measured from each image tile using the linear intercept method, corrected for 2D sectioning. With stable microscope conditions, errors in the automated measurements were found to be within 3% [22]. Electron Back Scatter Diffraction (EBSD) orientation mapping was performed across the HAZ banded layers using a CamScan Maxim FEG-SEM fitted with an Oxford instruments EBSD system, using a 0.3  $\mu\text{m}$  step size, and 20 kV accelerating voltage. The results here are depicted with IPF colouration with respect to the build direction (z).

Chemical analysis maps and line scans were performed using a JEOL JXA-8530F FEGEPMA equipped with 4 Wave Dispersive Spectrometers (WDS) and an Energy Dispersive Spectrometer

(EDS). Large area, 2.56 × 13.8 mm, (512 × 2760 pixel) signal intensity maps were first taken at 20 kV and 550 nA, using a 30 ms dwell time and 5  $\mu\text{m}$  step size, to detect regions of composition variation (using Fe - K $\alpha_1$  on LIFL and V- K $\beta_1$  on PETL diffraction crystals) and Al - K $\alpha_1$  by EDS. Quantification line scans were then performed by WDS at 9 kV, with the Fe (K $\alpha_1$ ) and V (K $\beta_1$ ) data taken using a 286 nA probe current and Al (K $\alpha_1$ ) at 181 nA. For higher resolution, site-specific, chemical analysis TEM specimens were extracted using a Focused Ion Beam (FIB) and analysed in a Technai G20 TEM with an EDX detector. The concentration of V and Al in the  $\alpha$  and  $\beta$  phases were measured using line scans with a step size of 10 nm across pre-selected microstructural morphologies at systematic positions relative to a HAZ band.

### 3. Results

#### 3.1. Overview

Typical optical macroscopic cross sections from the WAAM deposits are presented in Fig. 1. The most immediately obvious features in these etched samples are the commonly observed HAZ bands [8,11,20,31–34], which are 'written over' the coarse columnar prior- $\beta$  grain structure that can be seen in the background. In the transverse cross section views (z - y) the HAZ bands are virtually parallel in the single pass wide wall, but curved in the multi-pass wall. This occurs because in the single pass wall the peak temperature isotherms generated by the heat source translation are approximately parallel at the depth of the first HAZ band [16,17]. In comparison, in the multi-pass wall asymmetry in the thermal field develops when the melt pool tracks are overlapped laterally, as well as vertically. In the single bead wide wall the HAZ bands are approximately 1.3 mm in separation, which corresponds to the average added-layer height, and the first HAZ band appears at a depth equivalent to between four and five added layers (Fig. 1(b)): i.e. the translation of the heat source that deposited the last layer fully  $\beta$ -heat treated the material deposited previously to a depth of approximately 4.5 added layers.

On closer examination of the optical images in Fig. 1(b), in addition to the HAZ bands, curved weaker-contrast white etched lines can also be observed (arrowed) below the first HAZ band. It should be noted that this type of banding has not previously been widely reported and is difficult to reveal by etching. It is more obvious when seen against the horizontal darker-etched HAZ bands in the lower part of the sample (Fig. 1(d)). Very weak curved lines with the same profile are also apparent in the top fully  $\beta$ -annealed region of the wall, where they appear with slightly darker contrast (arrows Fig. 1(b)). This second form of banding is consistent with the predicted position of the fusion boundary from each melt track [16,17]. A similar weak fusion boundary etching effect has also been noted in Ti64 Gas Tungsten Arc (GTA) welds [37].

At higher magnification (Fig. 1(d)) it can be seen that when moving up vertically (in the build direction, z) the contrast in the HAZ bands becomes progressively darker and then changes to a narrower white line, before returning to the background contrast; i.e. the HAZs consist of a lower dark and higher thinner white band. This suggests that with height position within a HAZ band there is a progressively stronger and then more sudden weaker interaction with the Kroll's reagent during etching. In comparison, the thinner 'fusion boundary' band position appears to etch white against the darker matrix HAZ background.

The typical thermal history measured in a WAAM build for a sequence of five added layers is shown in Fig. 2. The peak temperature reached reduces with each addition cycle, but does not drop below the  $\beta$  transus (~1000 °C) until the 4th pass, although the peak temperature for the 4th heating cycle is very close to the  $\beta$

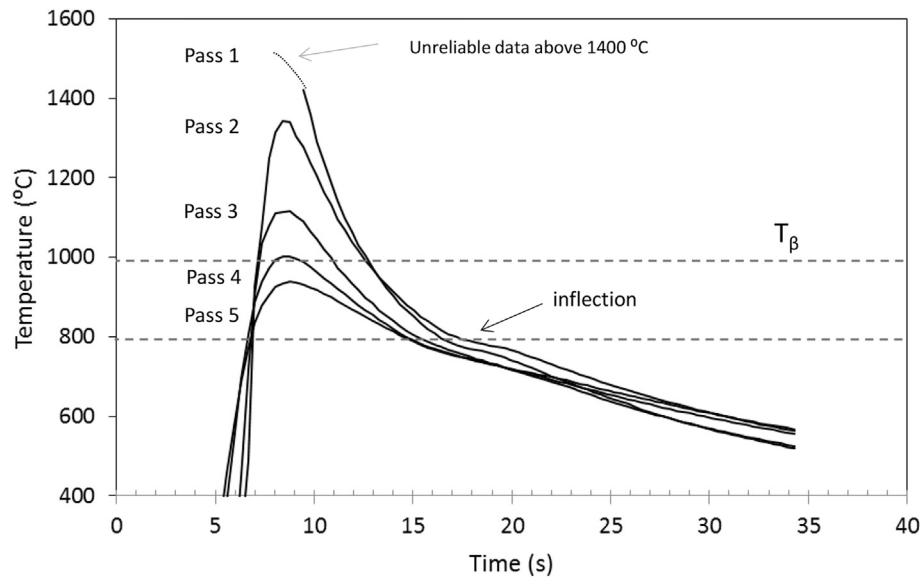


**Fig. 2.** The typical thermal history for 5 added layers in a WAAM build, taken from a thermocouple plunged into the weld pool at the centre of the single bead wide wall. (Note the curves have been shifted with the return time removed to aid comparison).

transus. Furthermore, an inflection is apparent in the cooling curves at around 800 °C, which can be associated with the highest rate of transformation to  $\alpha$  where the maximum rate of enthalpy release will occur. Fig. 2 also indicates that the time the material spends above the  $\beta$  transus temperature is only around 2–5 s per heating cycle. Apart from in the first pass, when the thermocouple was initially plunged into the melt pool and the data was unreliable, it can be further seen that the heating rates diminished in each consecutive thermal cycle from 800 to 250 K s<sup>-1</sup>. The cooling rates measured across the temperature range where the  $\alpha$  transformation is expected (1000–800 °C) also reduced in each repeated cycle from 100 to 30 K s<sup>-1</sup>.

### 3.2. Macroscopic chemical analysis

Large area qualitative (x-ray intensity) EPMA maps are presented in Fig. 3(a) from the single bead wide wall shown in Fig. 1(b). This analysis was performed to attempt to corroborate Kelly and Kampe's original observation that there is no systematic micro-scale composition variation across HAZ bands in LMD samples [32]. The high elemental sensitivity of the EPMA instrument used has, however, provided for the first time evidence of both compositional banding and microsegregation, or coring, in a Ti64 AM sample. It should be noted that in Fig. 3(a)–(b) the intensity scales have been stretched for Al and V and the signal detector variation seen in the maps is strongest for Fe and relatively weak for V (less than 10% of the mean). The segregation of Al was particularly weak and only just identifiable in Fig. 3(a). The regularly spaced, curved, segregation bands seen in the EPMA results are thus significantly dilute in Fe and only slightly dilute in V, and indicate a very slight positive segregation of Al. The segregation bands can be directly correlated to the thin weak-etched fusion boundary bands seen in Fig. 1. In comparison, the weaker coring could only be detected with respect to Fe and less strongly for V. It is also noticeable in Fig. 3(b) that the coring of Fe is most visible in the final added layer and reduces with depth, although the stronger fusion boundary segregation bands persist through the full build height.

While these large area EPMA maps have revealed previously unseen solidification-related microsegregation effects, in agreement with Kelly and Kampe [32], no clear systematic micro-scale

composition variation can be seen across the positions of the horizontal thermal HAZ bands in Fig. 3(a), except where they coincided with a fusion boundary band. To obtain quantified compositional information, line scans were also performed over three solute-depleted (fusion boundary) segregation bands, positioned below the first HAZ band, using a lower accelerating voltage (9 kV) and plotted against build height in Fig. 3(c). The positions where the scans cross fusion boundaries or a HAZ bands are indicated in the figure. These higher resolution plots can be seen to be noisy due to scatter caused by the smaller interaction volume at 9 kV and the duplex  $\alpha$ - $\beta$  microstructure, which effected the relative proportion of V and Al at each probe position. Nevertheless, a significant drop in the Fe concentration can be clearly seen across each fusion boundary by about 50%, from 0.23 wt% to 0.11 wt%. In comparison, the behaviour of V and Al is harder to interpret. However, the fusion boundary bands appear to be consistently slightly lower in V and very slightly higher in Al. This can be seen more clearly across the fusion boundary at the centre of the line scan, which was furthest in proximity from a HAZ band. Data across this segregation band is shown enlarged at the right side of the plots in Fig. 3(c), where it can be seen that the V concentration has reduced from 3.8 to ~3.4 wt%, whereas Al has increased slightly from about 5.81 to 5.89 wt%. The results also suggest that there is greater scatter in the data when it crosses a HAZ band, which is affecting the results by partially masking the fusion boundary segregation. This behaviour will be discussed further below, but arises from microstructure coarsening and greater solute partitioning between  $\alpha$  and  $\beta$  in the HAZ bands, which increases the point to point variation in the measurements. Because of the real noise in the EPMA composition data caused by the dual phase microstructure we have also not been able to reliably measure the amplitude of the finer-scale, weaker, micro-segregation pattern, seen in the top-most layers.

### 3.3. $\alpha$ morphologies and inter-lamellar spacing measurements

In Figs. 4–7 results are presented that quantify the changes that occur in the transformation microstructure during repeated layer addition in the WAAM process. In Fig. 4(a) data from the automated  $\alpha$  lamellar spacing maps is plotted against build height (averaged from 5 wide image-tile maps) across the areas indicated in the

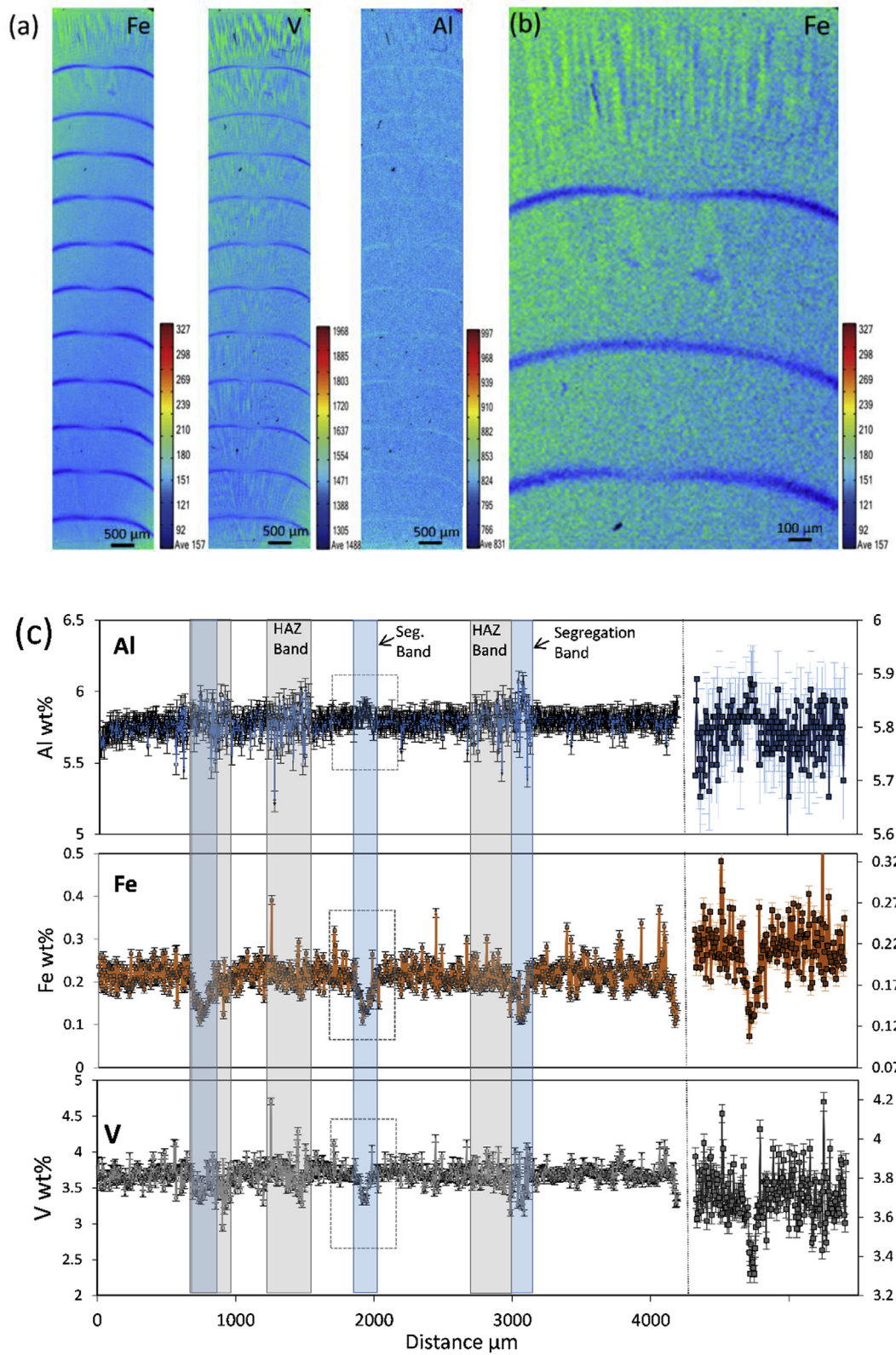


**Fig. 3.** Large area qualitative EPMA signal intensity maps, showing; (a) local variation in Fe and V by WDS and Al by EDS, and (b) the Fe distribution in the top three layers at a higher magnification (note; for V and Al the intensity scales have been stretched and there is much smaller variation than for Fe). In (c) quantified EPMA concentration profiles are shown across three fusion boundary segregation bands obtained at a depth just below the  $\beta$  re-annealed top layer. The positions of the HAZ and segregations bands are indicated. The central segregation band (dashed rectangle) where the data was not affected by proximity to a HAZ is enlarged at the right of each plot.



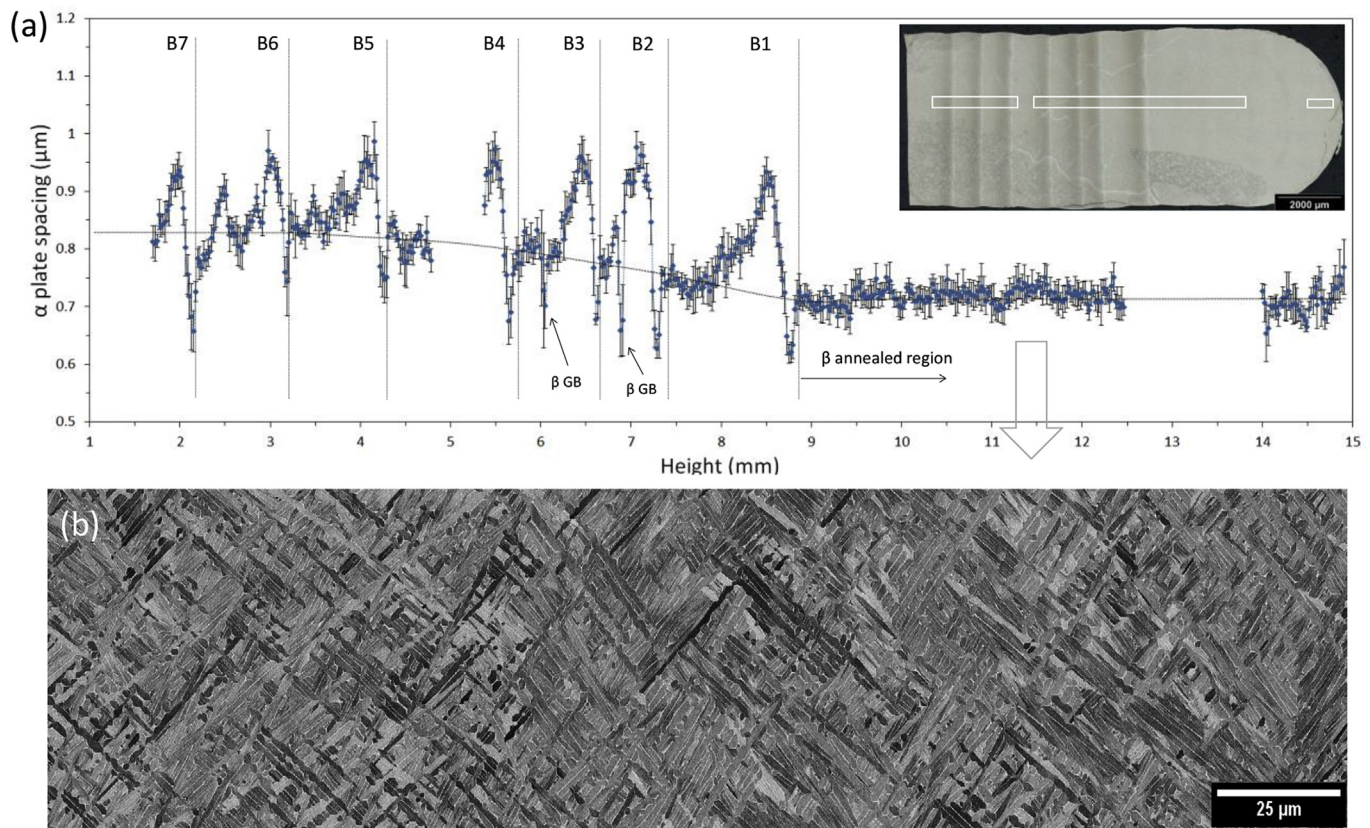


**Fig. 4.** (a) Linear intercept  $\alpha$  lamellar spacings averaged in the transverse direction, from stitched image tile maps in a single bead wide wall, taken from the positions indicated in the optical micrograph insert from the top  $\beta$ -annealed region of the wall down through 7 HAZ bands, along with (b) an example of the transformation microstructure seen in the top fully  $\beta$ -annealed region. The HAZ Bands are labelled B1–B7 from top to bottom.

insert. This analysis includes measurements from near the top surface and from above the first HAZ band, down through 7 HAZ bands (B1–7 in Fig. 4(a)). It can be seen that in the region above the first HAZ band (at the top of the deposit) the  $\alpha$  inter-lamellar spacing is very uniform, whereas on moving downwards across the HAZ bands it exhibits a regular wave-like periodicity, as well as an average background drift-increase which reaches a near steady-state plateau lower in the wall.

The top region above the first HAZ band shown in Fig. 4(b) can be seen to consist of a uniform Widmanstätten basketweave microstructure. The  $\alpha$  lamellar spacing across this region had an average spacing of  $\sim 0.73 \mu\text{m}$  and the measurements were consistent within a narrow range across the full height measured (Fig. 4(a)). This region was fully  $\beta$  annealed by the last pass of the heat source and did not experience any further thermal cycles [20,32]. The image in Fig. 4(b) also does not show any evidence of martensite formation, which is consistent with the measured cooling rates in Fig. 2 [24].

Below the position of the first HAZ band it can be seen in Fig. 4(a) that there is a drift upwards in the background  $\alpha$  lamellar spacing over the first four HAZ bands (B1–B4) which then appears to reach a steady state of  $\sim 0.83 \mu\text{m}$  (B5–B7). This suggests that longer thermal exposure and overlap of the HAZ bands from subsequent passes caused a general coarsening of the  $\alpha$  lamellar spacing, relative to when it first transformed in the last deposition pass in the fully  $\beta$  – annealed top region and not just where optical imaging shows dark HAZ etching contrast in Fig. 1(d).

A further plot is provided in Fig. 5(a) to highlight the characteristic ‘saw tooth’, wave-like, repeat pattern seen in the inter-lamellar measurements across each HAZ band in Fig. 4(a). This

data was taken from the top HAZ band (B1) in Fig. 4(a) and has also been linked to the systematic changes seen in the transformation microstructure, which are illustrated by SEM-BSE images in Fig. 5(b) – (g). Moving from left to right across the HAZ band in Fig. 5(a) is equivalent to an increasing peak temperature being reached in the thermal field from the last pass of the heat source and, as one might expect, the  $\alpha$  plate spacing increases correspondingly from the background level. More surprisingly, accurate quantification reveals that when the lamellar spacing reaches a maximum in Fig. 5(a) it then drops very suddenly in a narrow transient layer to a minima of  $\sim 0.65 \mu\text{m}$ , which is less than the background level, before rising again to complete the next repeat cycle.

Comparison between Figs. 5 and 1(d), indicates that the dark-etching portion of the HAZ band corresponds to where there is a significant increase in the lamellar spacing and this becomes darker in contrast the greater the extent of coarsening; whereas the narrow region, where a sudden dip occurs and a very fine  $\alpha$ -lamellar spacing is seen, corresponds to the thinner white-etched layer at the top of each HAZ band.

From the SEM images in Fig. 5(b) – (g) it can be observed that the ‘saw tooth’ repeat pattern in  $\alpha$ -lamellar spacing across each thermally affected band is associated with distinct changes to the transformation microstructure. Moving up through each layer (from left to right in Fig. 5(a)) the ‘background’  $\alpha$  (Fig. 5(b)) between the etched HAZ bands can be seen to have a basketweave morphology, similar in appearance to that at the top of the build. This microstructure then coarsens markedly (Fig. 5(c)–(d)) as the peak temperatures rises and the contrast between the  $\beta$  and  $\alpha$  in the BSE images also increases, suggesting greater partitioning of V

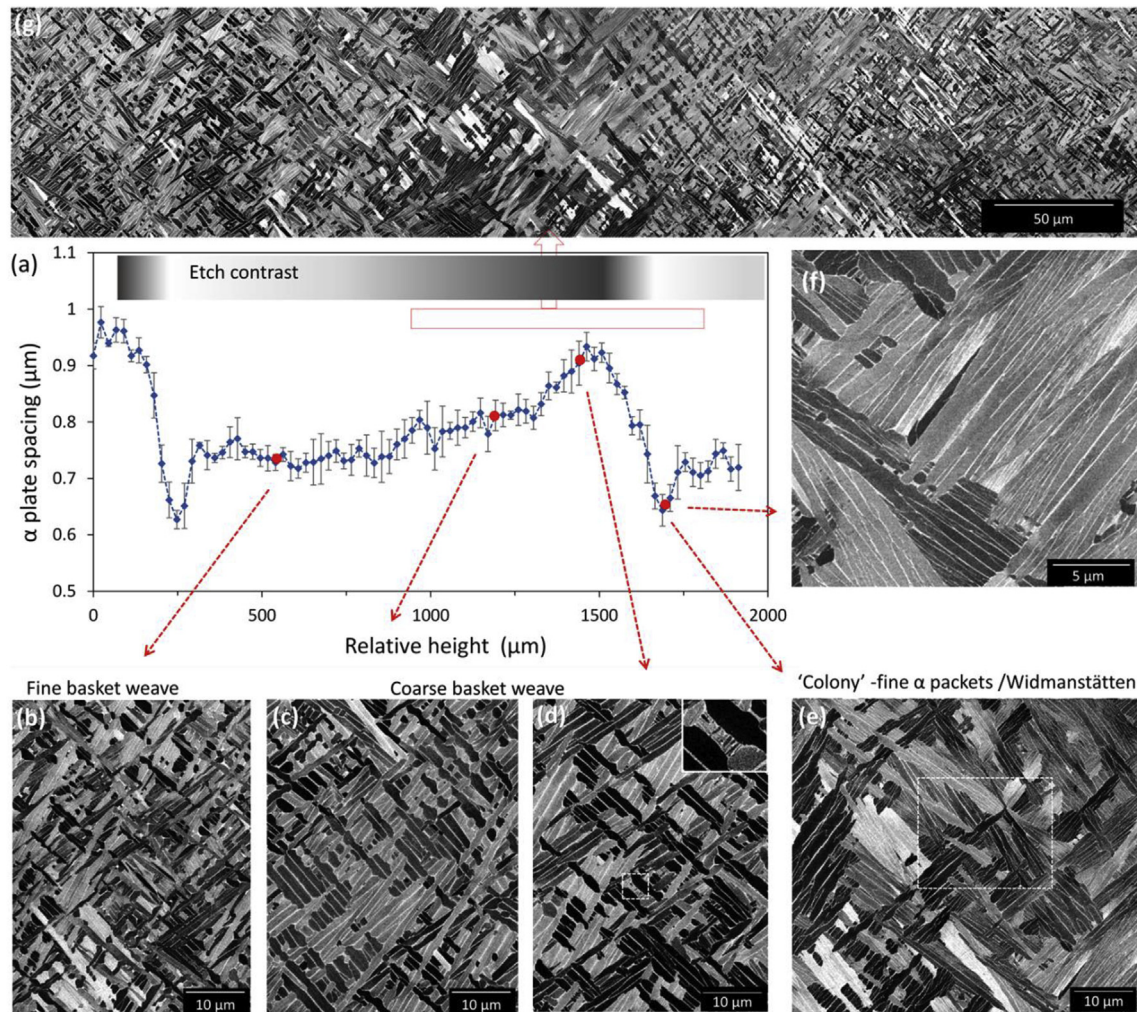


**Fig. 5.** (a) The characteristic 'saw tooth' - like repeat pattern seen across each HAZ band in Fig. 4(a), plotted with sequential example SEM-BSE images, showing; (b) the fine basketweave microstructure seen between each HAZ band, (c)–(d) the coarsened basketweave microstructure within each dark etched HAZ layer, and (e) the thin transition zone of very fine  $\alpha$  in larger single-variant packets, or 'colonies', taken from the white etched HAZ layer, with (f) an enlargement of (e). The insert in (d) provides evidence of secondary  $\alpha$  within the coarsened region. In (g) the dramatic change across the white etched transition zone is highlighted in a single image tile strip.

and Al, but an overall a similar basketweave morphology is maintained. Very occasionally small regions of secondary  $\alpha$  were also seen in the most heavily coarsened region (insert in Fig. 5(d)). Finally, in the white-etched layer where the  $\alpha$  inter-lamellar spacing dropped abruptly in Fig. 5(a), there is a sudden change in  $\alpha$  morphology to larger packets of much finer single variant, or a more 'colony-like', microstructure (Fig. 5(e)–(f)). The microstructural sequence through this abrupt transition, which is repeated as each new layer is added, is also apparent in the coarser scale image tile strip provided in Fig. 5(g).

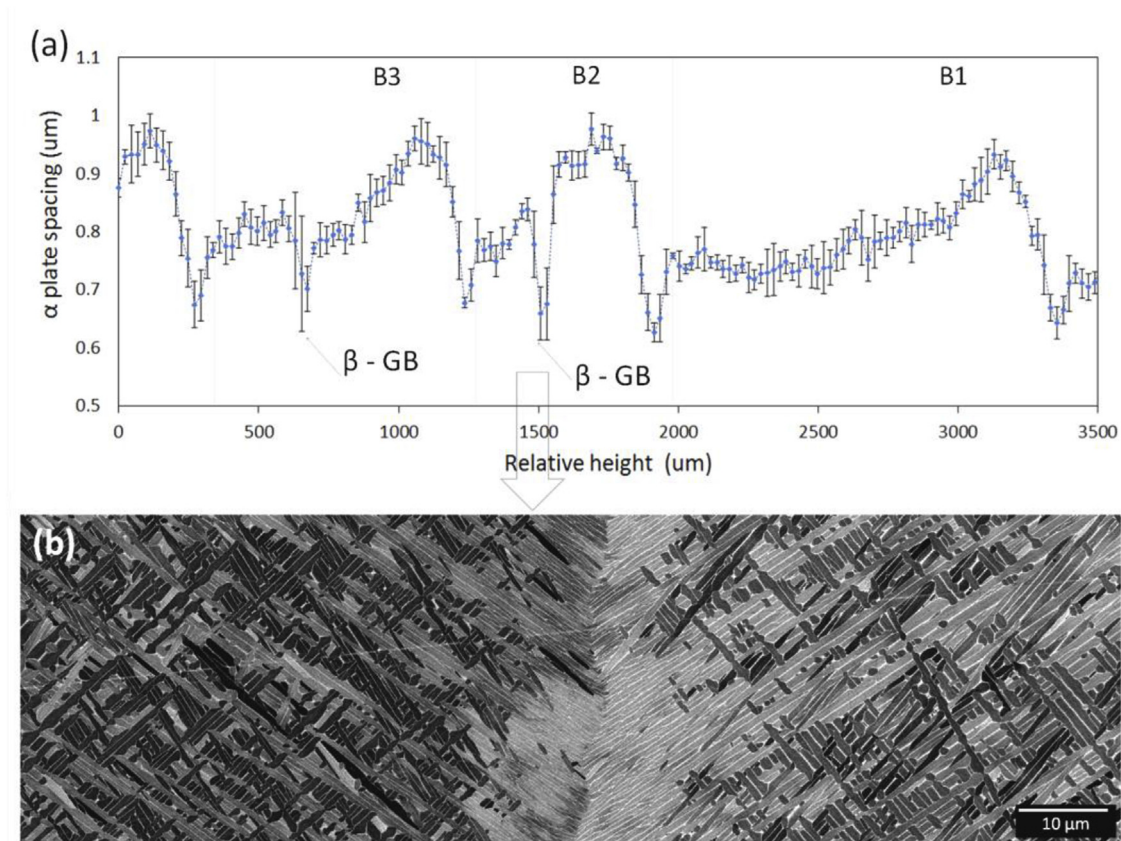
Finally, it should be noted that the repeat pattern described above is subject to a number of anomalies. As can be seen in Fig. 4(a), the added layer height was not completely regular, which affected the relative thermal field overlap. When this overlapped more strongly the background lamellar spacing between HAZ bands tended to be greater. In addition, a number of sharp dips in  $\alpha$  lamellar spacing were seen between some HAZ bands, where the spacing suddenly reduced to a similar level to that found in the troughs associated with the thin colony-like microstructure layer. An example of this behaviour is highlighted Fig. 6. These minima positions were identified as coinciding with where the image tile strip crossed a transverse  $\beta$ -grain boundary (labelled as  $\beta$ -GBs in

Fig. 6(a)). It can be seen in Fig. 6(b) that in the region of the prior  $\beta$  grain boundary there is an  $\alpha$  colony layer, which extends into the grain either side of the  $\beta$  boundary by about 15  $\mu\text{m}$ . The local crystallography has not been analysed, but the appearance suggests that there is a preferential orientation relationship between the variants in each colony that have nucleated from the same  $\beta$  grain boundary [38]. Due to the high cooling rate in the WAAM process, the  $\alpha$  colonies do not extend far into the  $\beta$  grains because they are in competition with the basketweave microstructure that nucleated within the matrix. However, it can be seen in Fig. 6(b) that each colony consists of a single  $\alpha$  variant that grew with a finer average lamellar spacing than the surrounding basketweave microstructure; when averaged in the transverse direction across the image tiles their presence thus produced the additional minima seen in lamellar spacing in Fig. 6(a).

### 3.4. EBSD $\alpha$ 'grain' size analysis

Because of the presence of regions with a different  $\alpha$  packet, or 'colony', size in the HAZ banded layers, EBSD micro-texture analysis has been used to measure the effective local  $\alpha$  grain size. For this analysis the average area within the perimeter of a single  $\alpha$





**Fig. 6.** (a) Linear intercept  $\alpha$  lamellar spacing across HAZ bands B1–B3, highlighting the position where the image map crosses two transverse  $\beta$  grain boundaries (marked  $\beta$ -GB); (b) SEM image of the fine colony microstructure seen across the transverse boundary indicated in (a).

orientation (with a misorientation spread of  $1.5^\circ$ ) was measured as a function of build height across the transition where the microstructure changed most rapidly, from the peak coarsened basketweave  $\alpha$ , through to the region with the finest  $\alpha$  spacing, and then back to the background lamella width. The results are shown in Fig. 7 and confirm that the thin layer where the lamella spacing was finest is associated with a marked increase in the size of a single  $\alpha$ -variant packet.

### 3.5. $\alpha$ - $\beta$ Solute partitioning

As etching is strongly affected by chemistry, a higher resolution approach was employed to further investigate the possibility of finer-scale composition variation from solute partitioning. Chemical analysis was performed using a Tecnai T20 TEM equipped with an EDX detector, on thin foils FIB milled from specific positions across a typical HAZ band. The spatial resolution of the measurements was  $\sim 4$  nm, which was finer than that of the retained  $\beta$  phase. From Fig. 8 it can be observed in the sample with the fine background microstructure, taken from between the HAZ etch bands where limited coarsening had occurred, that the  $\beta$  phase contained around 10% V, whereas in the coarsest  $\alpha$  lamellar region it had a higher V content of above 20%. Finally, the  $\beta$  phase in the very fine colony white etching microstructure was found to contain only around 6–7% V (Fig. 8(c)). In comparison, less difference was measured between the sample positions in the Al concentration in the  $\alpha$  phase, but this again was found to be lowest in the fine colony  $\alpha$  and greatest in the coarse basketweave samples. Overall, the results thus show that solute partitioning was closer to equilibrium in the re-heat treated, coarsened,  $\alpha$  microstructure, lower in the

background transformation microstructure, and least in the white etched very fine colony structure seen at the top of each HAZ band.

## 4. Discussion

Two separate deposition-related microstructure banding features have been identified in the Ti64 WAAM samples that are characteristic of AM processing: namely HAZ bands, which have been well documented [8,11,20,31–34], and less reported solute segregation bands. Both features have been quantified in far more detail than previously. In the process we have also highlighted a greater degree of composition variation in the as-deposited AM Ti64 samples than has been hitherto published [30]. The two types of bands are formed essentially independently at different depths, as each new layer is added, but it is useful to discuss them in the order they occur so that any potential interaction between them can be considered.

### 4.1. Fusion boundary solute depletion layer and microsegregation

The thinner, weak-etching, bands of solute segregation shown in Fig. 1 and analysed in Fig. 3, suggests a strong association with a solidification process. The profile of the etch line is very similar to the melt pool shape predicted by FE simulations of a single bead wide WAAM deposit [16,17] and comparable etching effects have been observed at the fusion boundary in stainless steel AM samples [39]. Elmer et al. [37] have also reported a similar weak contrast fusion boundary etch line in Ti64 GTA weld micrographs. In addition, this band is similar to the ‘inter-layer band’ feature reported by Zhu et al. [34] in a Ti-6.5Al–3.5Mo–1.5Zr alloy deposited by LMD,

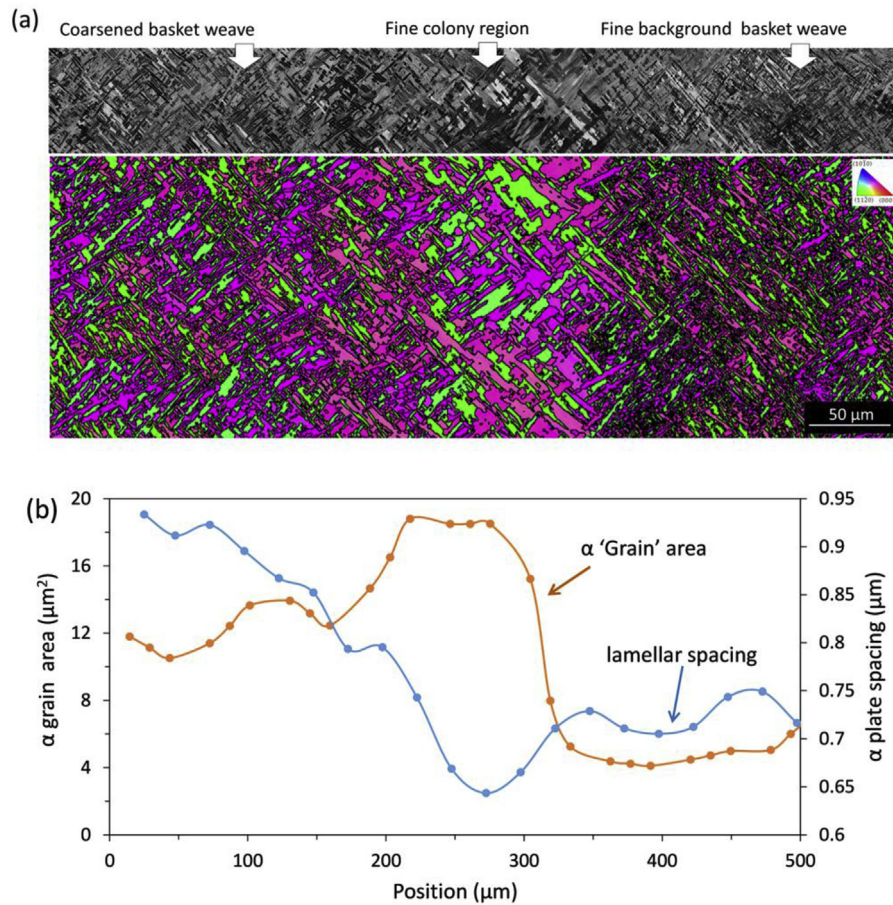


**Fig. 7.** (a) EBSD  $\alpha$  (IPF contrast relative to  $z$ ) orientation map and (b) the accompanying average  $\alpha$  'grain area' and lamellar spacing, plotted against position across the region within a HAZ band where the microstructure changes most rapidly, from the coarsened maximum  $\alpha$  plate spacing, through the narrow layer with a minimum lamellar spacing and larger single  $\alpha$ -variant 'colony' size, back to the fine background basketweave microstructure.

where the presence of Mo ( $k = 2$  [28]) would be expected to cause a more obvious segregation effect.

Because this type of banding is closely associated with the expected profile of the fusion boundary, it is most likely to be caused by an initial transient response when the solid-liquid interface reverses from retreating, on melting ahead of the melt pool, to advancing - during solidification at the rear of the melt pool. For example, simple constant velocity planar front solidification models with limited diffusion in the solid predict an initial transient behaviour in the solid phase before the steady state liquid composition profile develops at the solidification front [40,41]. In this scenario the solid phase is first expected to freeze with a composition  $k_0 C_0$  [41]. Fe, which has the lowest partition coefficient (Table 2), will thus be the most strongly affected element - in agreement with the EPMA line scans. However, in a moving melt pool scenario the solidification rate at the fusion boundary accelerates from zero as the heat source translates [39] and this more complex situation would benefit from further investigation.

Thermodynamic assessment of the respective binary phase diagrams for V and Al with Ti [42,43] suggests there is a marginal difference between the liquidus and solidus compositions at 4% V and 6% Al and the partition coefficients ( $k$ ) in both cases are close to 1 [28], within the range of the error in experimental data. In the Ti-Al system 6 wt% Al (10 at%) is also very close to a saddle point where  $L \leftrightarrow \beta_{Ti}$  at 1690 °C [43]. In Table 2, as well as the theoretical binary partition coefficients [28], we have presented values of  $k$  determined from a multicomponent calculation using the commercial

Calphad software JMatPro™, for the bulk average alloy composition, with a nominal oxygen content of 0.1 wt%. These predictions give  $k_V = 0.97$ , and  $k_{Al} = 1.15$  and a slightly lower value for Fe of  $k_{Fe} = 0.35$ , compared to 0.38 in the binary system [28]. For Al a very slight positive segregation was observed in the EPMA maps, which was difficult to quantify, but in Fig. 3(d) can be seen to be ~2%. The maximum local reduction of solute measured here in Fig. 3(b) for V was also small, being about 10% and this could be accounted for by a partition coefficient of the order of 0.9, which is slightly lower than that predicted. In comparison the local iron concentration was measured as 0.11, relative to a background of 0.22 wt%, which suggests less segregation than that expected from a partition coefficient of  $k_{Fe} \sim 0.35$ . However, using experimental measurements from casting experiments Birmingham et al. [27] have also noted a smaller deviation and obtained an experimental value of  $k_{Fe}$  of 0.79. Using this value of  $k_{Fe}$  gives a predicted reduction to 0.18 wt% Fe, which gives less segregation than that measured. Overall, this suggests the unusually high diffusion rate of Fe [44,45] may be reducing the level of segregation, either by back diffusion during solidification or by homogenisation during subsequent thermal cycling.

In the enlarged EPMA map in Fig. 3(b) significant coring of iron was evident in the last two layers deposited, although the because the segregation is very weak it is not very clear if this caused by a cellular or dendritic microstructure. Interestingly, the diffusion coefficient for Fe is known to be unusually high in  $\beta$ -Ti, because of its partial interstitial character [44], and is nearly 2 orders of



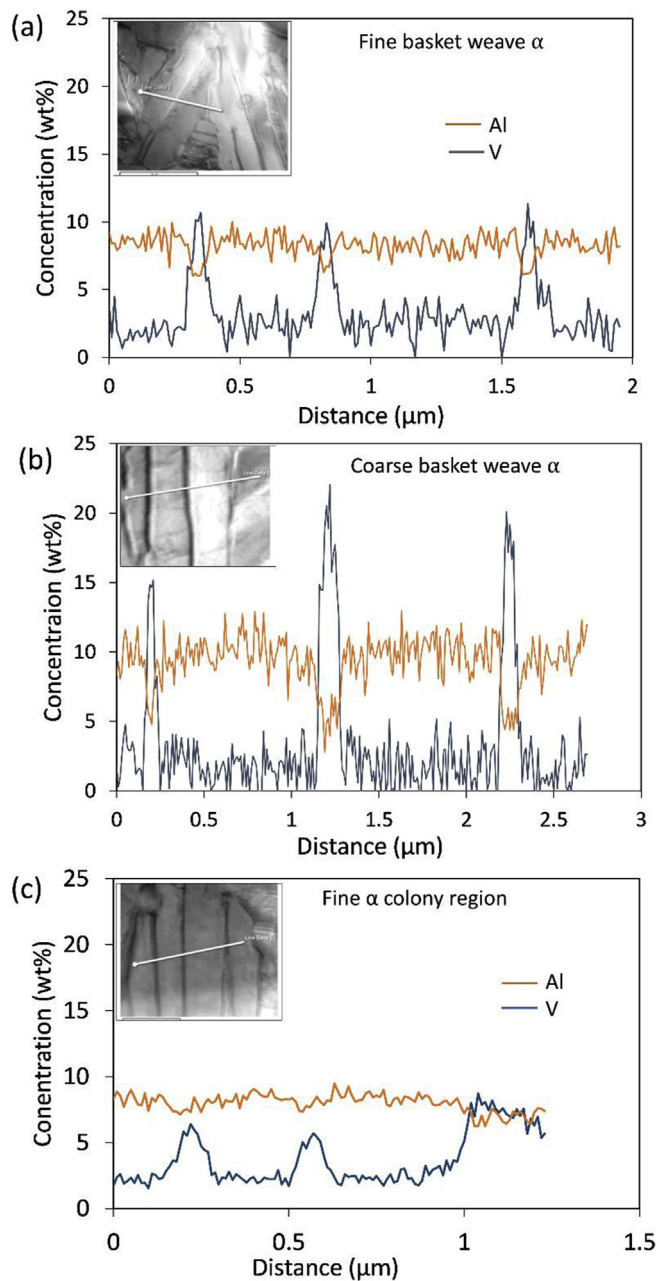


**Fig. 8.** TEM - EDX line scans across  $\alpha$  -  $\beta$  lamellar from specific positions across a HAZ band, using site-specific samples extracted by FIB: (a) the fine background  $\alpha$  lamellar region, (b) the coarsest  $\alpha$  lamellar region and (c) the very fine 'colony'  $\alpha$  region.

**Table 2**

Partition coefficients,  $k$ , from Ref. [28] for binary Ti-X, systems and calculated from JMatPro™ for a Ti-6%Al-4%V-0.15%Fe-0.1%O alloy. Data is also provided for the approximate inter-diffusion coefficients in  $\beta$  Ti at 1200 °C for Al and V from Takahashi et al. [47] and Fe from Nakajima et al. [45].

Element	$C_0$ (wt%)	$k$ (binary)	$K$ (JMatPro)	$k_{JMP} \cdot C_0$	$D_{1200C}$ ( $\text{cm}^2\text{s}^{-1}$ )
Al	6	$\approx 1$	1.15	1	$1 \times 10^{-9}$ [47]
V	4.1	$\approx 1$	0.97	3.9	$0.8 \times 10^{-9}$ [47]
Fe	0.15	0.38	0.35	0.05	$2 \times 10^{-7}$ [45]

magnitude higher than for Al and V (Table 2) [45–47]. Thus, Fe will tend to homogenise much more readily when the deposition passes from subsequent layers reheat the previously deposited layers into

the  $\beta$  phase field and this may explain why the microsegregation of Fe seen in the top layer in Fig. 3(b) diminishes further down in a build, whereas that for V does not. This could also explain why the segregation in the transient fusion boundary band is lower than expected from the theoretical value of  $k_{Fe}$ .

Overall, it should be recognised that Fe is a trace element and the segregation of V and Al seen on solidification is a weak effect and is, therefore, unlikely to have any major consequences for the mechanical performance of AM parts. The results also show that in the majority of the WAAM deposit the  $\beta$ -phase can be considered to be nearly chemically homogenous before transformation to the typical Widmanstätten microstructure found at room temperature, apart from where there is slight dip in the V and Fe concentration in the thin, localised, fusion boundary bands. To explore further if any influence of fusion boundary solute banding could be detected on the local transformation microstructure, BSE image mapping was carried out across the boundary of the last layer deposited. As Fe and V are  $\beta$  stabilisers and Al is an  $\alpha$  stabiliser, segmentation was performed to see if there was a reduction in the  $\beta$  volume fraction across the band. In Fig. 9 the resultant averaged  $\beta$  volume fractions are shown along with example binarized images. The results indicate a small reduction in the average  $\beta$  volume fraction of the order of  $\sim 20\%$  at the position of the segregation band, which coincides with a slight increase in the  $\alpha$  lamellar spacing ( $\sim 8\%$ ). This local reduction in  $\beta$  volume fraction is consistent with the equilibrium change calculated from JMatPro™ (12.7–10.2% at 750 °C).

#### 4.2. HAZ banding

In Ti64 AM the HAZ banding seen in etched optical images has been much more widely reported in the literature (e.g. Refs. [8,11,12,20,31–34,48]) and is related to similar heat affected zones seen in welding [49]. However, the cyclic re-heating that occurs in AM when multiple layers of material are added sequentially can make interpretation more complex (e.g. Refs. [31–34]) (Fig. 2). Interpretation can be can also be affected by debate surrounding martensite formation. Fortunately, in WAAM martensite is not expected owing to the lower cooling rates ( $<100 \text{ K s}^{-1}$ ) [24] and all the microstructures we have observed are consistent with a diffusional transformation; i.e. a V enriched  $\beta$  phase was always observed in the BSE SEM images. Following the TEM chemical analysis, the characteristic etching pattern seen moving up through a HAZ in optical images (Fig. 1(d)) of a gradual increase in dark contrast, followed by a thin white less-etched layer at the top of each HAZ band, can now be attributed to the change in solute partitioning between the  $\alpha$  and  $\beta$  phases, which increases as the microstructure coarsens and then reduces again to a minimum in the very finer colony layer seen at the top of each band: i.e. an increase in the chemical disparity between the  $\alpha$  and  $\beta$  phases, combined with the increase in scale of the  $\alpha$  lamellar, will lead to stronger differential etching and darker contrast in an optical image.

The first comprehensive description of the material response in HAZ bands in a DMD process was provided by Kelly and Kampe [32,33], under a slightly higher cooling rate regime to WAAM in LMD samples, where they observed that the  $\alpha$  lamellar spacing coarsened in the HAZ band from a background (mid layer) of  $1 \mu\text{m}$ – $1.5 \mu\text{m}$  and was finest immediately above the HAZ band ( $0.9 \mu\text{m}$ ). Kelly and Kampe further noted a fine 'colony-like' microstructure at the top of each HAZ band, they suggest appears on re-heating to temperatures just above the  $\beta$  transus. Their data is thus consistent with the higher resolution quantitative results presented in Figs. 4–6. Morphological and local texture changes have also subsequently been noted across HAZ bands by other authors and attributed to the peak temperature, time at

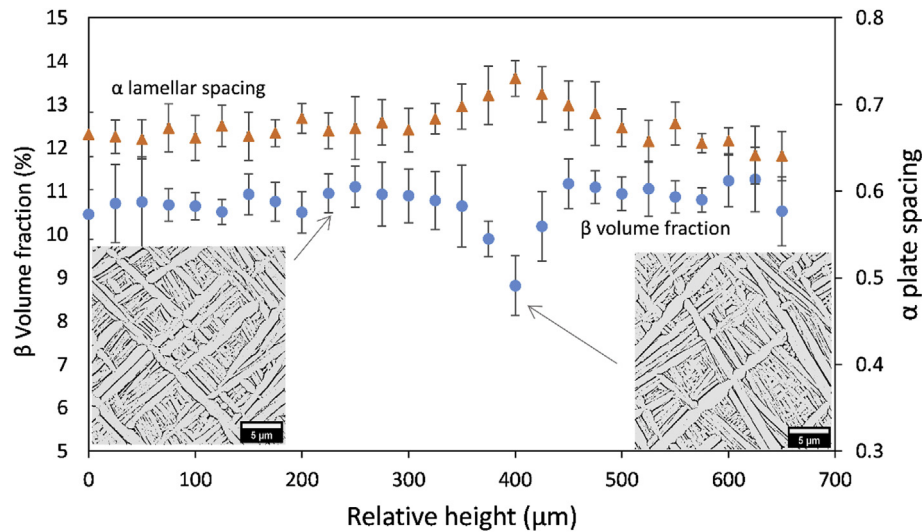


**Fig. 9.** The  $\beta$  phase volume fraction and  $\alpha$  lamellar spacing measured across the fusion boundary of the last layer to be deposited, measured from image tile maps. Example binarized images are shown as inserts.

temperature, and cooling rate affecting competition between different  $\alpha$  microstructures [12,19,20,32,33,48]. Kelly and Kampe have suggested coarsening of the transformation microstructure occurs at peak temperatures greater than that at which the  $\alpha$  phase first starts to ‘dissolve’ in favour of  $\beta$  re-growth [32]; i.e. within the regime of the  $\beta$  transus approach curve. Here, however, there is little evidence of competing diffusionless transformations and the scenario that produces the HAZ bands seen in the WAAM material is less complex than that envisaged by Kelly and Kampe, with the exception of explaining the presence of the fine colony microstructure which will be discussed further below.

In a single melt track-wide wall the final HAZ band is generally assumed to appear at a position below the top surface where the peak temperature rise is approximately equivalent to the  $\beta$ -transus temperature ( $T_\beta$ ) [12,20,32,33]. Modelling has shown that the isotherms generated by the heat source at this depth are approximately parallel in the x-y plane due to the high aspect ratio geometry and large temperature interval between the melting point and  $\beta$  transus ( $\sim 700^\circ\text{C}$ ) [16,17], which leads to the parallel-linear banding seen in Fig. 1(b). Although the region above the first HAZ band is typically cycled into the  $\beta$ -phase field up to 5 times, as additional layers are added, this region is formed in the last deposition pass when it all cooled from above  $T_\beta$  with a similar cooling rate [16,17]. The transformation microstructure present above the final HAZ band was consequently found to be remarkably uniform (Fig. 4). When a new layer is then added the heat source is incremented upwards and the region above the previous HAZ zone is  $\beta$ -annealed to the same depth as before, with an accompanying new HAZ drawn on the fully  $\beta$ -annealed transformation microstructure produced in the previous pass. In each pass the heat source will increment upwards a distance equivalent to the added layer height, so that the  $\beta$ -transus isotherm generated by the heat source will move the same distance and the spacing between each new HAZ is thus equivalent to the layer height. This process is shown schematically in Fig. 10, against a fully  $\beta$  annealed starting microstructure.

In WAAM due to the high cooling rate and coarse  $\beta$  grain size the transform microstructure produced prior to a HAZ band forming is predominantly Widmanstätten basketweave, although a thin grain boundary  $\alpha$  allotriomorphic layer is commonly observed [19], which can nucleate a narrow region of single-variant colony  $\alpha$  at

the  $\beta$  grain boundaries (Fig. 6). As discussed by Radhakrishnan et al. [50], in AM where there is a large prior  $\beta$  grain size and high cooling rate, grain boundary  $\alpha$  nucleation will saturate at an early stage and the colony structure will grow inwards too slowly to transform the majority of a  $\beta$  grain before the undercooling becomes high enough to promote  $\alpha$  nucleation within a grain.  $\alpha$  nucleation occurs first in the  $\beta$  parent matrix in the strain field of dislocations and then autocatalytically, within the strain field of growing  $\alpha$  plates, to form a limited number of variants that become interwoven to produce the basketweave morphology, which is in competition with the GB colony microstructure [50].

Radhakrishnan et al. [50] have further suggested that the colony microstructure reported by Kelly and Kampe may appear just above  $T_\beta$  because it is affected by the dislocation density, which arises from the relaxation of residual stresses and this would reduce with distance from the fusion boundary, thus favouring a colony relative to basketweave microstructure when the dislocation density falls below a critical level. We have, however, found the  $\alpha$  lamellar microstructure to be remarkably uniform in the top fully  $\beta$  annealed region of the build (Fig. 4) and it can also be noted that when the first HAZ band formed it was at a considerable distance below the fusion boundary, so that the highly localised thin colony  $\alpha$  layer observed at the top of each HAZ band is unlikely to have been produced by a gradient in dislocation density.

Because the time at temperature is very short in an AM thermal cycle (Fig. 2), the rapid coarsening of the basketweave microstructure in the HAZ bands has been reported to be associated with the temperature above which the  $\beta$  phase volume fraction starts to increase significantly [8,12,20,30–34,48], although the mechanism responsible for this behaviour has not been previously discussed. The  $\beta$  transus approach curve obtained from JMatPro is plotted in Fig. 11(a) and predicts that under equilibrium conditions the  $\beta$  phase volume fraction only starts to re-grow significantly above  $\sim 700^\circ\text{C}$  and then increases rapidly above  $800^\circ\text{C}$ , until full transformation to  $\beta$  occurs. Fig. 11(a) also shows that, although the equilibrium composition of the  $\beta$ -phase is strongly dependent on temperature, the  $\alpha$ -phase composition does not vary as greatly, in agreement with the TEM EDX results in Fig. 8. However, it is possible that the  $\beta$ -transus temperature may shift to higher temperatures with the high heating rates found in WAAM [37], which will affect the position of the HAZ bands relative to the heat source



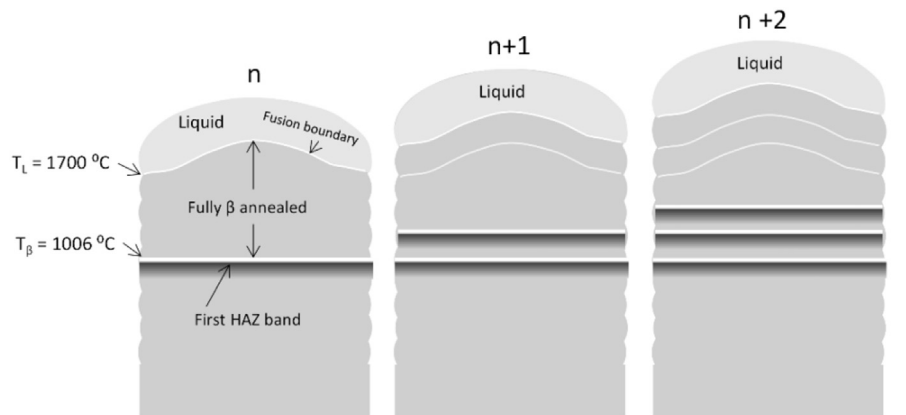


**Fig. 10.** Schematic diagram showing the development of banded layers within a single track wide WAAM wall, against a fully  $\beta$  annealed starting microstructure.

thermal field.

To first explore this possibility, dilatometer results are presented in Fig. 11(b) where the position of the  $\beta$ -transus temperature has been measured from the change of slope. The results are plotted as

a function of heating rate in the range relevant to the WAAM process and show that  $T_\beta$  increased to 1006 °C, at  $632 \text{ K s}^{-1}$ , relative to 983 °C for the slow heating rate reference of  $0.5 \text{ K s}^{-1}$ . It can therefore be concluded that there is a small increase in  $T_\beta$  in the

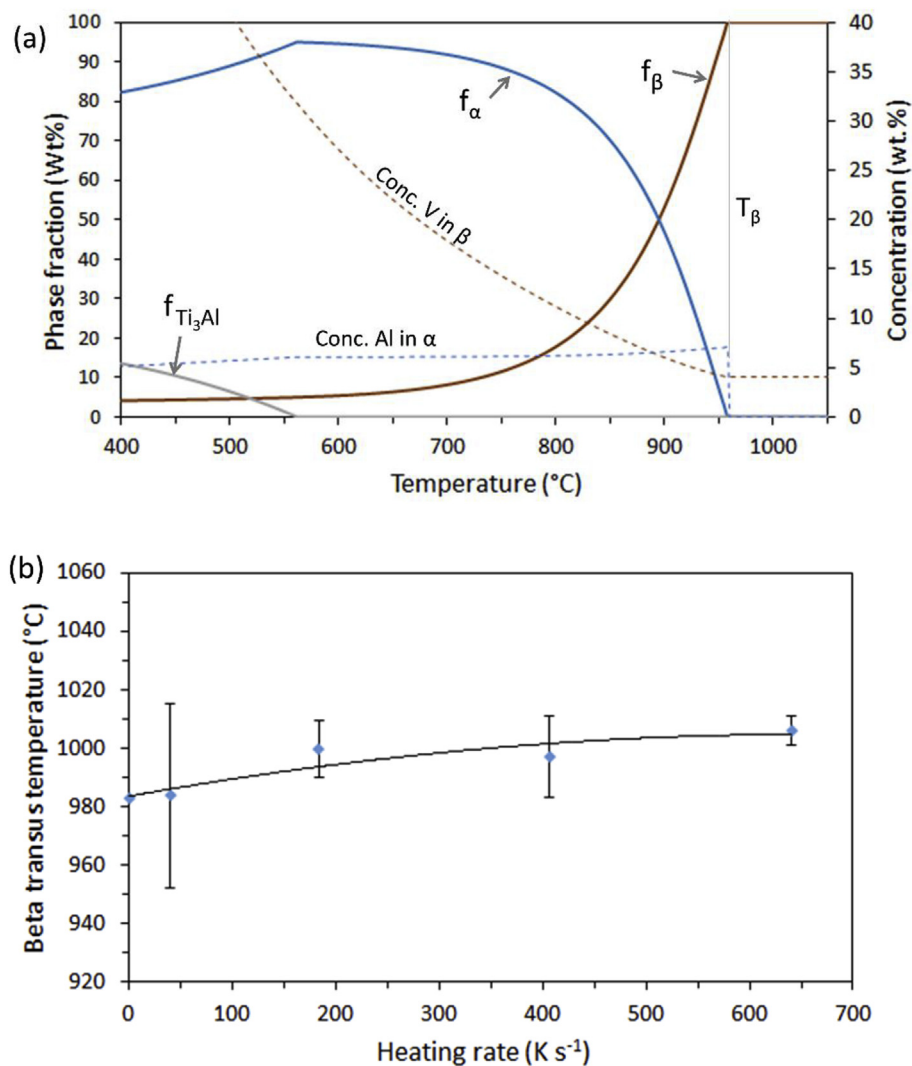


**Fig. 11.** CALPHAD predictions from JMatPro™ (a) of the  $\alpha$  and  $\beta$  phase equilibrium weight fractions and Al and V concentrations with temperature, with accompanying dilatometer results (b) showing the shift in the  $\beta$  transus temperature with heating rate, measured in the range 0.5–632  $\text{K s}^{-1}$ .

heating rate regime relevant to the WAAM process of about 24 °C. This relatively small shift can be attributed to the fact that on heating the  $\beta$ -phase regrows from the retained inter-lamellar  $\beta$  and there is not a requirement for nucleation with an associated energy barrier. The transformation kinetics will thus be controlled by the migration velocity of the  $\alpha/\beta$  interfaces. Interface mobility will also accelerate with increasing temperature, due to the rising driving force and diffusivity and because of the fine nature of the starting transformation microstructure the distance that an interface has to move to increase the  $\beta$  volume fraction is also small ( $<0.5\ \mu\text{m}$  to achieve 100%  $\beta$ ). If equilibrium at the growth front is maintained, the rate limiting step will be partitioning of V which is the slowest diffusing species [51] (Table 2).

The increase in  $T_\beta$  with heating rate, noted above, suggests that at these high heating rates  $\beta$  re-growth may occur without the equilibrium V concentration necessarily being maintained. It can be seen from Fig. 8(a) that when the transformation microstructure first formed (fine background basketweave morphology) the measured V concentration of  $\beta$  is  $\sim 10\ \text{wt}\%$  and for Al in  $\alpha$  is  $\sim 7\ \text{wt}\%$ , which agrees well with the predictions of the phase compositions in Fig. 11(b) at the measured temperature of maximum transformation rate;  $\sim 800\ ^\circ\text{C}$ . In contrast, the  $\beta$ -phase in the coarsened lamellar microstructure was measured to have a higher V content of  $\sim 20\ \text{wt}\%$ . This would suggest that by coarsening the  $\beta$  phase achieved a closer to equilibrium V concentration at a predicted equivalent temperature from Fig. 11(a) of  $\sim 700\ ^\circ\text{C}$ ; or, as this temperature is relatively low in the  $T_\beta$  approach curve, during cooling and thermal cycling at lower temperatures in subsequent passes more partitioning of V has occurred.

#### 4.2.1. HAZ band coarsening behaviour

It should be recognised that when rapidly heating towards the  $\beta$  transus temperature in Ti coarsening of a lamellar two phase microstructure is not primarily caused by conventional Ostwald ripening; i.e. it is not driven just by a reduction in interfacial energy, which is a second order effect relative to the higher free energy change associated with the  $\alpha - \beta$  phase transformation. The mechanism proposed is shown schematically in Fig. 12(a) and occurs as a result of the retained  $\beta$  re-growing and increasing its volume fraction with increasing temperature. If  $\beta$  re-growth, controlled by interface mobility, occurs uniformly then the thinnest  $\alpha$  plates within the size distribution of the original transformation microstructure will grow out first, due to impingement of the thickening inter-lamellar  $\beta$  matrix. On cooling, as the temperature falls, the  $\alpha - \beta$  interface of the coarser  $\alpha$  plates that survived the heating cycle will then reverse their direction of migration and the  $\alpha$  plates will grow back, consuming the  $\beta$  matrix. If the distance between the  $\alpha$  plates that survive is still relatively small, an undercooling sufficient to nucleate more  $\alpha$  ahead of the growth front will not be achieved and a coarsened lamellar microstructure will therefore be observed at room temperature. This mechanism is thus linked to the increase in volume fraction of  $\beta$  seen with rising peak temperature and will lead to more rapid coarsening than interfacial energy-driven Ostwald ripening, in agreement with the qualitative observations by many authors that  $\alpha$  HAZ band coarsening occurs in the temperature regime defined by the  $\beta$  - transus approach curve [12,20,31–34,48].

Further validation of the above analysis is presented in Fig. 13, where simulations were performed in the dilatometer with the same heating and cooling rate as found in the WAAM process of 800 and  $30\ \text{K s}^{-1}$ , respectively. The sample shown in the first image (a) was heated to  $1100\ ^\circ\text{C}$ , which is above the  $\beta$ -transus temperature measured at this heating rate ( $1006\ ^\circ\text{C}$ , Fig. 11(b)), and shows a basketweave microstructure similar to that seen in the  $\beta$  annealed top layer of the WAAM sample (Fig. 4(b)). In comparison the

samples in Fig. 13(b) and (c) were re-heated to peak temperatures of 900 and  $950\ ^\circ\text{C}$  and show increased coarsening of the lamellar microstructure with the same basketweave morphology, similar to in Fig. 5(b)–(d). In contrast, sample (d) in Fig. 13 was heated to a similar peak temperature to (c), but held for 3 s and then cooled at over twice the cooling rate ( $80\ \text{K s}^{-1}$ ). In this case it can be seen that the microstructure has a similar primary  $\alpha$  lamellar spacing, to in Fig. 13(c), but now there is clear differentiation between the primary  $\alpha$ , which has partially regrown on cooling, and a surrounding matrix of finer secondary  $\alpha$  that formed when a higher undercooling rate was used. In addition, it is apparent that in alloys where  $\alpha/\beta$  interface migration rate is slower, such as in the work of Zhu et al. [34] owing to the presence of a slow diffusing species like Mo, it is more likely that differentiation between primary and secondary  $\alpha$  will be observed within HAZ bands. Here, in the WAAM samples secondary  $\alpha$  was only observed rarely within small areas of the re-grown  $\beta$  matrix in the most coarsened region of the HAZ bands (Fig. 5(d) insert). Small regions of secondary  $\alpha$  have also been reported by Baufeld et al. [8] in laser-wire Ti64 AM samples.

#### 4.2.2. The fine colony $\alpha$ morphology

The observation that the top of each HAZ band is associated with a thin white-etching band comprised of a fine  $\alpha$  lamella structure with a larger single-variant packet size (or a fine colony layer) has not been previously clearly explained. Kelly and Kampe [32,33] have suggested this layer could be linked to locally different cooling rates for peak temperatures just above  $T_\beta$ , while Radhakrishnan et al. [50] have proposed it may be related to a gradient in dislocation density in the  $\beta$  grains and occurs when the dislocation site density available for  $\alpha$  nucleation falls below a critical level. Thus, the first key question to answer is if this morphological band forms on re-heating to peak temperatures above, or below, the  $\beta$  transus temperature. We have, therefore, performed thermal simulations to try to replicate this microstructure transition, correlated to a known peak temperature rise.

In Fig. 13(e) an example micrograph is shown from a dilatometer simulation that looks identical to the fine lamellar colony  $\alpha$  microstructure seen in Fig. 5(f), which was obtained by heating to a peak temperature of  $980\ ^\circ\text{C}$  with the replicated WAAM heating and cooling rates of 600 and  $30\ \text{K s}^{-1}$ . It should be noted that rapid induction heating does not produce a completely uniform sample temperature - so there is some uncertainty in the peak temperature. However, all the samples were sectioned close to the control thermocouple position, where the temperature is expected to be within  $10\ ^\circ\text{C}$  of that measured. By performing repeated experiments it was found that the fine lamellar colony  $\alpha$  microstructure could only be consistently replicated within a narrow temperature range of  $970\text{--}1000\ ^\circ\text{C}$  and for lower peak temperature rises (Fig. 13(b) and (c)) only coarsening of the normal basketweave transformation microstructure were seen, as described above., whereas for higher peak temperatures a conventional fully basketweave microstructure was produced (e.g. Fig. 13(a)).

If the shift in the  $\beta$ -transus temperature to  $1006\ ^\circ\text{C}$  at WAAM heating rates (which was measured in the same instrument used for the thermal simulations) is taken into account (Fig. 11(b)) these results thus show that the fine  $\alpha$  colony microstructure layer is formed in a narrow temperature range just below the  $\beta$ -transus temperature, where there is a small volume fraction of retained  $\alpha$ . From Fig. 11(a), if the difference in the predicted and measured  $T_\beta$  is taken into account, at this temperature the residual  $\alpha$  can be estimated to be less than 5%. A scenario can thus be envisaged depicted schematically in Fig. 12(b) where, as the temperature rises and the matrix  $\beta$  volume fraction increases, the distances between surviving  $\alpha$  plates will eventually become too large, such that on rapid cooling the increasing driving force will favour break down of the



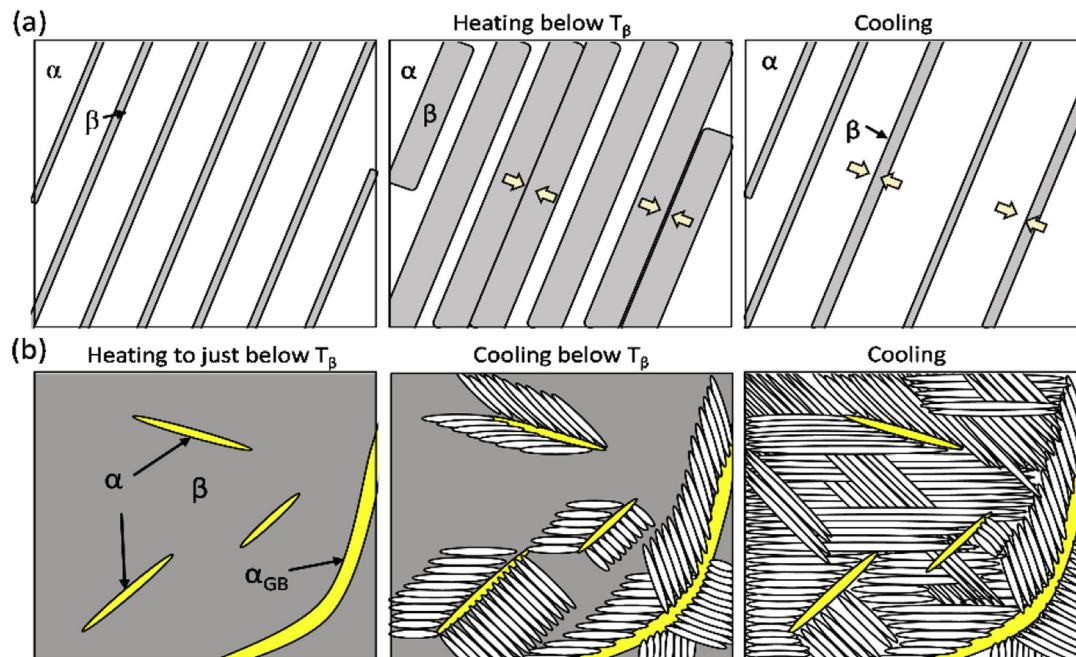


**Fig. 12.** Schematic diagrams illustrating possible formation mechanisms for the HAZ band microstructures; (a) coarsening of the  $\alpha$ – $\beta$  lamellar transformation microstructure, (b) formation of the fine  $\alpha$  colony microstructure.

growth front, by single variant  $\alpha$  colonies being nucleated from surviving  $\alpha$  plates; i.e. the  $\alpha$  colony morphology is heterogeneously nucleated from a low volume fraction of surviving  $\alpha$  plates and is therefore seen within a narrow band in the WAAM walls, which can be associated with a small temperature range of  $\sim 35^\circ\text{C}$  below  $T_\beta$ . This would also explain the comparable appearance of the HAZ colony  $\alpha$  layer to that of the grain boundary colony  $\alpha$  seen in the same sample (Fig. 6).

An obvious flaw in the above argument is that the surviving primary  $\alpha$  plates might be expected to be visible in the microstructure with a distinctly different plate size. To date we have not been able to distinguish primary  $\alpha$  plates within the complex transformation structure, and this is probably because the thermal cycle is too fast to allow sufficient growth of the surviving  $\alpha$  plates to produce an obvious enough size differential. In comparison, when using a higher cooling rate (e.g. Fig. 13 (e)) and in a more  $\beta$  stabilised alloy (Ti–6.5Al–3.5Mo–1.5Zr–0.3Si) re-heating to a high temperature in a HAZ band layer can result in a bimodal microstructure containing identifiable primary  $\alpha$  [32]. It is also, perhaps, surprising that the  $\alpha$  lamellar plate spacing seen in the colony microstructure layer was finer than found in the fully  $\beta$ -annealed basketweave microstructure. In this context it is noteworthy that grain boundary  $\alpha$  colonies observed in the WAAM material had a similarly lower lamellar spacing (Fig. 6(a)). While furthering understanding of the difference in the lamellar spacing that forms between the colony microstructure and the basketweave  $\alpha$  at high cooling rates is beyond the scope of this paper, it is not unexpected that under continuous cooling conditions growth of a single  $\alpha$  variant in a colony will produce a different optimum lamellar spacing to nucleation and growth of interwoven  $\alpha$  variants within a basketweave microstructure.

#### 4.3. Overall influence of HAZ banding

In the Ti64 WAAM samples the top layer that was fully  $\beta$  annealed in the final heat source pass had a more uniform and finer

average  $\alpha$  lamellar spacing than seen in the HAZ banded region lower down in the steady state section of the deposit (Fig. 4). The underlying background lamellar in between the HAZ bands region was also found to increase below the first HAZ, to a plateau level lower in the wall that was slightly higher than in the top fully  $\beta$ -annealed region (from 0.73 to 0.83  $\mu\text{m}$ ). This longer range drift of the lamellar spacing can be attributed to the layer height being such that there was some overlap of the HAZ generated during adding each new layer and there is also the possibility that with increasing build times residual heat will lead to a slow lower temperature coarsening response. This behaviour is much more pronounced in powder bed AM processes, such as EBM, where there is more overlap of the thermal fields from multiple beam passes and where a higher ambient temperature is purposely maintained for long exposure times, so that much greater microstructure coarsening occurs [22,23,52]. Thus, despite the much lower cooling rate in WAAM deposits the average  $\alpha$  plate spacing's are still finer on average and the yield strength competitive with powder bed EBM [20,23,52].

Nevertheless, as the steady state HAZ banded region will form the majority of a final machined component, the repeated thermal cycling involved in HAZ banding is important as it will influence the average lamellar spacing and the practical yield strength achievable in a WAAM deposit [52]. In addition, HAZ bands containing substantially coarsened  $\alpha$  lamellar would be expected to increase anisotropy and affect more localised mechanical properties, such as the propagation of fatigue cracks. For example, crack deflection by HAZ bands in WAAM samples has been noted in fatigue tests [30]. The thin colony microstructure band will also have a larger potential slip line length, which may contribute to further mechanical heterogeneity [19,21].

#### 5. Conclusions

The microstructure banding found in samples produced by Wire-Arc Additive Manufacturing (WAAM) have been quantified in

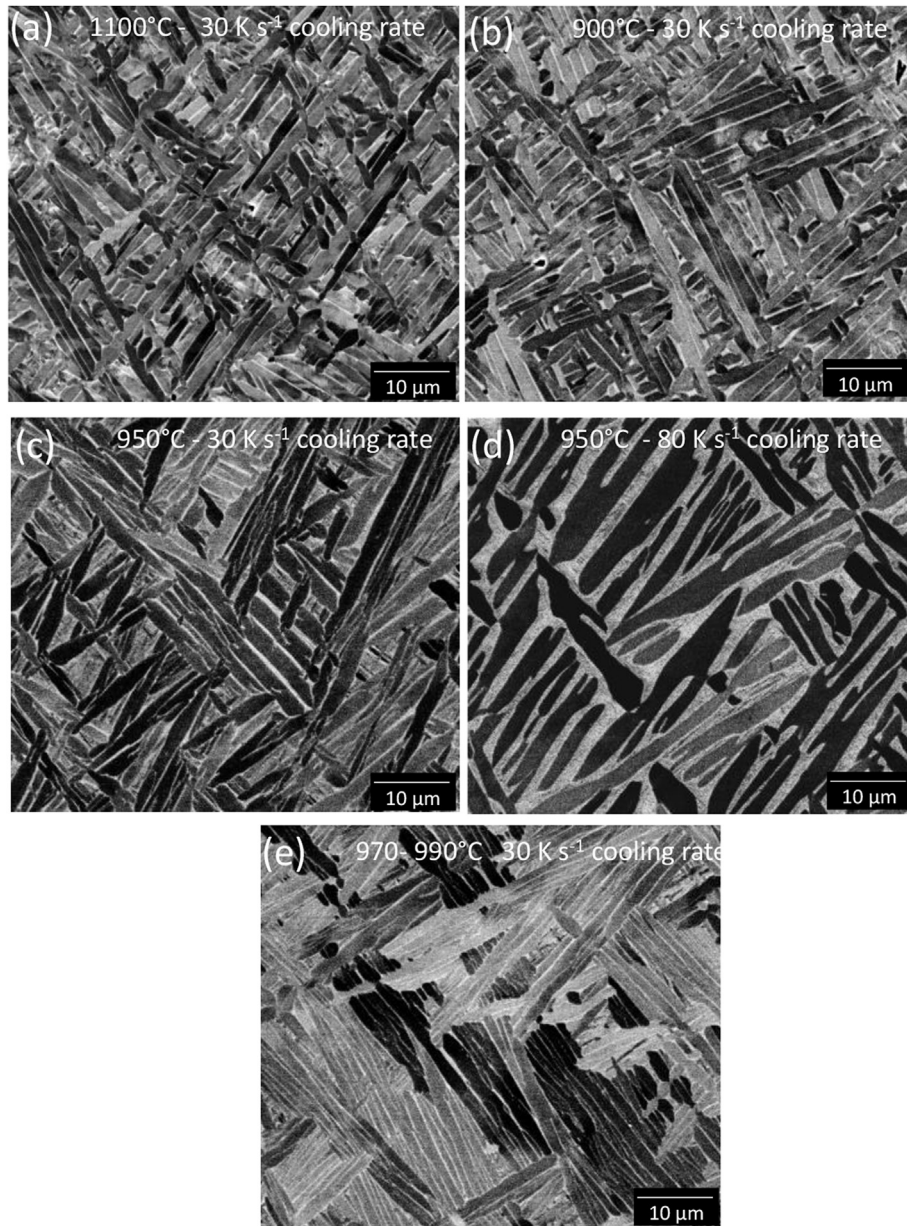


**Fig. 13.** Microstructures obtained by simulations performed in the dilatometer with the same heating and cooling rate as found in the WAAM process (400 and  $30\text{ K s}^{-1}$ , respectively); (a) heated to  $1100^\circ\text{C}$ , slightly above the  $\beta$  transus, (b) and (c) re-heated to peak temperatures of 900 and  $950^\circ\text{C}$  showing increased coarsening, (d) heated to a similar temperature to (c), held longer (for 3 s), and cooled with double the rate and (e) heated to a peak temperature just below  $T_\beta$  of  $980^\circ\text{C}$ .

greater detail than previously, using both multiscale compositional and automated image mapping tools. In addition to more fully explaining the origin of the commonly reported HAZ banding seen in AM Ti64 parts, this approach has revealed, for the first time, a segregation layer at the fusion boundary from each melt track and evidence of weak microsegregation during solidification.

The fusion boundary segregation bands can be attributed to the development of a transient solute boundary layer at the solidification front when it first accelerates. This was a relatively weak effect with respect to the main alloying elements Al and V, but significant with respect to Fe, owing to its lower partition coefficient. The fusion boundary segregation bands were found to locally influence the transformation microstructure by reducing the  $\beta$  phase stability. Weak microsegregation, or coring, of Fe and V were also observed within the deposits. The microsegregation of Fe was,

however, noted to become more homogenised deeper in a build due to the greater thermal exposure and Fe's unusually high diffusivity in Ti.

In the fully  $\beta$ -annealed top region of a deposit the transformation microstructure was found to consist of a uniform basketweave lamellar  $\alpha$  morphology, confirming that this region all cooled with a similar rate from above  $T_\beta$  in the final deposition pass.

The dark and white etching contrast regions seen in optical images of each HAZ band have been shown to be caused by a complex behaviour involving coarsening of the transformation microstructure, accompanied by greater  $\alpha$  -  $\beta$  solute partitioning, which etches dark, and the formation of a microstructurally distinct, thin, colony layer at the top of each HAZ band, with a finer lamellar structure, that exhibits less solute partitioning and etches white. This behaviour is shown to result in a repeating 'saw-tooth'

like  $\alpha$  lamellar spacing profile across each HAZ band.

A small shift in the  $\beta$  transus temperature was found at the high heating rates experienced in the WAAM process, from 983 to 1006 °C. When this effect was taken into account, the presence of the thin colony morphology white layer at the top of each HAZ band was demonstrated, by thermal simulation, to be consistent with a peak temperature rise just below the  $\beta$ -transus temperature.

Coarsening of the lamellar transformation structure seen within each dark HAZ band occurred in the temperature range of 700–960 °C, up to a  $\beta$  volume fraction of ~95%. However, it is proposed that the coarsening process involved is better described by transformation coarsening, from migration of the  $\alpha/\beta$  interfaces during re-growth of the  $\beta$  phase, which consumes individual  $\alpha$  plates that then do not reform on cooling, rather than by a conventional interfacial energy driven process. The change to an  $\alpha$  colony microstructure with a finer lamellar spacing that resulted in the appearance of a thin white band at the top of each HAZ (in the temperature range of 960 °C to 1006 °C) has been attributed to the nucleation of packets of single  $\alpha$  variants, during cooling, on the low density of  $\alpha$  plates that survived re-heating at temperatures just below the  $\beta$  transus.

Overall, the quantitative microstructure mapping has shown that HAZ banding and the degree of overlap of the thermal field from each melt track is an important consideration in AM with wire-based high deposition rate processes, as it effectively controls the average  $\alpha$  lamellar spacing in the majority of a final component and will therefore influence its strength and mechanical heterogeneity.

## Acknowledgements

The authors are appreciative of the EPSRC's (grants LightForm - EP/R001715/1; NEWAM - EP/R027218/1), Innovate UK (Open Architecture Additive Manufacturing, OAAM) and the Metallic Systems CDT (EP/L016273/1) for supporting aspects of this research. Professor P.B. Prangnell is also grateful to the Royal Academy of Engineering, UK and Airbus Operations UK for financial support.

## Appendix A. Supplementary data

Supplementary data to this article can be found online at <https://doi.org/10.1016/j.actamat.2018.12.038>.

## References

- [1] W.J. Sames, F.A. List, S. Pannala, R.R. Dehoff, S.S. Babu, The metallurgy and processing science of metal additive manufacturing, *Int. Mater. Rev.* 61 (5) (2016) 315–360.
- [2] D. Herzog, V. Seyda, E. Wycisk, C. Emmelmann, Additive manufacturing of metals, *Acta Mater.* 117 (2016) 371–392.
- [3] D.L. Bourell, Perspectives on additive manufacturing, *Annu. Rev. Mater. Res.* 46 (2016) 1–18.
- [4] T. DebRoy, H.L. Wei, J.S. Zuback, T. Mukherjee, J.W. Elmer, J.O. Milewski, A.M. Beese, A. Wilson-Heid, A. De, W. Zhang, Additive manufacturing of metallic components – process, structure and properties, *Prog. Mater. Sci.* 92 (2018) 112–224.
- [5] D. Ding, Z. Pan, D. Cuiuri, H. Li, Wire-feed additive manufacturing of metal components: technologies, developments and future interests, *Int. J. Adv. Manuf. Technol.* 81 (2015) 465–481.
- [6] C. Körner, Additive manufacturing of metallic components by selective electron beam melting – a review, *Int. Mater. Rev.* 61 (5) (2016) 361–377.
- [7] W.E. Frazier, Metal additive manufacturing: a review, *J. Mater. Eng. Perform.* 23 (6) (2014) 1917–1928.
- [8] B. Baufeld, E. Brandl, O. van der Biest, Wire based additive layer manufacturing: comparison of microstructure and mechanical properties of Ti–6Al–4V components fabricated by laser-beam deposition and shaped metal deposition, *J. Mater. Process. Technol.* 211 (2011) 1146–1158.
- [9] K.M.B. Taminger, R.A. Hafley, Electron beam freeform fabrication for cost effective near-net shape manufacturing, *NATO AVT- 139* (16) (2006) 1–10.
- [10] J. Gockel, J. Beuth, K. Taminger, Integrated control of solidification microstructure and melt pool dimensions in electron beam wire feed additive manufacturing of Ti–6Al–4V, *Addit. Manu.* 1–4 (2014) 119–126.
- [11] F. Martina, P.A. Colegrove, S.W. Williams, J. Meyer, Microstructure of interpass rolled wire + arc additive manufacturing Ti–6Al–4V components, *Metall. Mater. Trans.* 46A (12) (2015) 6103–6118.
- [12] F. Martina, J. Mehnen, S.W. Williams, P. Colegrove, F. Wang, Investigation of the benefits of plasma deposition for the additive layer manufacture of Ti–6Al–4V, *J. Mater. Process. Technol.* 212 (2012) 1377–1386.
- [13] T. Duda, L.V. Raghavan, 3D Metal Printing Technology, vols. 49–29, IFAC-PapersOnLine, 2016, pp. 103–110.
- [14] C. Petrey, Norsk Titanium Charts the Future of Flight, *Modern Metals*, August 2018, <http://www.modernmetals.com>.
- [15] I.A. Roberts, C.J. Wang, R. Esterlein, M. Stanford, D.J. Mynors, A three-dimensional finite element analysis of the temperature field during laser melting of metal powders in additive layer manufacturing, *Int. J. Mach. Tool Manufact.* 49 (12–13) (2009) 916–923.
- [16] V.D. Fachinotti, A. Cardona, B. Baufeld, O. Van der Biest, Finite-element modelling of heat transfer in shaped metal deposition and experimental validation, *Acta Mater.* 60 (2012) 6621–6630.
- [17] X. Bai, P. Colegrove, J. Ding, X. Zhou, C. Diao, P. Bridgeman, J.R. Hönnige, H. Zhang, S.W. Williams, Numerical analysis of heat transfer and fluid flow in multilayer deposition of PAW-based wire and arc additive manufacturing, *Int. J. Heat Mass Tran.* 124 (2018) 504–516.
- [18] J. Donoghue, A.A. Antonysamy, F. Martina, P.A. Colegrove, S.W. Williams, P.B. Prangnell, The effectiveness of combining rolling deformation with wire–arc additive manufacture on  $\beta$ -grain refinement and texture modification in Ti–6Al–4V, *Mater. Char.* 114 (2016) 103–114.
- [19] P. Åkerfeldt, M.-L. Antti, R. Pederson, Influence of microstructure on mechanical properties of laser metal wire-deposited Ti–6Al–4V, *Mater. Sci. Eng., A* 674 (2016) 428–437.
- [20] Wang, S.W. Williams, P. Colegrove, A.A. Antonysamy, Microstructure and mechanical properties of wire and arc additive manufactured Ti–6Al–4V, *Metall. Mater. Trans.* 44 (2013) 968–977.
- [21] G. Lütjering, J.C. Williams, *Titanium*, Springer, 2007.
- [22] H. Zhao A. Ho, A. Davis, A.A. Antonysamy, P.B. Prangnell, Automated image mapping and quantification of microstructure heterogeneity in additive manufactured Ti6Al4V Materials, *Character* 147 (2018) 131–145.
- [23] S. Al-Bermani, M. Blackmore, W. Zhang, I. Todd, The origin of microstructural diversity, texture, and mechanical properties in electron beam melted Ti–6Al–4V, *Metall. Mater. Trans.* 41 (2010) 3422–3434.
- [24] T. Ahmed, H.J. Rack, Phase transformations during cooling in  $\alpha$ - $\beta$  titanium alloys, *Mater. Sci. Eng., A* 243 (1–2) (1998) 206–211.
- [25] A.A. Antonysamy, J. Meyer, P.B. Prangnell, Effect of build geometry on the  $\beta$ -grain structure and texture in additive manufacture of Ti–6Al–4V by selective electron beam melting, *Mater. Char.* 84 (2013) 53–168.
- [26] J.A. Koepf, M.R. Gotterbarm, M. Markl, C. Körner, 3D multi-layer grain structure simulation of powder bed fusion additive manufacturing, *Acta Mater.* 152 (2018) 119–126.
- [27] M.J. Bermingham, S.D. McDonald, D.H. StJohn, M.S. Dargusch, Segregation and grain refinement in cast titanium alloys, *J. Mater. Res.* 24 (2009) 1529–1535.
- [28] M.J. Bermingham, S.D. McDonald, M.S. Dargusch, D.H. St John, Grain-refinement mechanisms in titanium alloys, *J. Mater. Res.* 23 (1) (2008) 97–104.
- [29] R.G. Ding, Z.W. Huang, H.Y. Li, I. Mitchell, G. Baxter, P. Bowen, Electron microscopy study of direct laser deposited IN718, *Mater. Char.* 106 (2015) 324–337.
- [30] X. Zhang, F. Martina, J. Ding, X. Wang, S.W. Williams, Fracture toughness and fatigue crack growth rate properties in wire + arc additive manufactured Ti–6Al–4V, *Fatigue Fract. Eng. Mater. Struct.* 40 (2017) 790–803.
- [31] P.A. Kobryn, S. Semiatin, Microstructure and texture evolution during solidification processing of Ti–6Al–4V, *J. Mater. Process. Technol.* 135 (2–3) (2003) 330–339.
- [32] S.M. Kelly, S.L. Kampe, Microstructural evolution in laser-deposited multilayer Ti–6Al–4V builds: Part I. microstructural characterization, *Metal Metall. Mater. Trans.* A 35 (2004) 1861–1867.
- [33] S.M. Kelly, S.L. Kampe, Microstructural evolution in laser-deposited multilayer Ti–6Al–4V builds: Part II thermal modelling, *Metall. Mater. Trans.* 35 (2004) 1869–1879.
- [34] Y. Zhu, X. Tian, J. Li, H. Wang, Microstructure evolution and layer bands of laser melting deposition Ti–6.5Al–3.5Mo–1.5Zr–0.3Si titanium alloy, *J. Alloy. Comp.* 616 (2014) 468–474.
- [35] H. Zhao, Microstructure Heterogeneity in Additive Manufactured Ti–6Al–4V, PhD Thesis, the University of Manchester, 2016.
- [36] J. Canny, A computational approach to edge detection, *IEEE Trans. Pattern Anal. Mach. Intell.* PAMI- 8 (6) (1986) 679–698.
- [37] J.W. Elmer, T.A. Palmer, S.S. Babu, W. Zhang, T. DebRoy, Phase transformation dynamics during welding of Ti–6Al–4V, *J. Appl. Phys.* 95 (12) (2004) 8327–8339.
- [38] D. Bhattacharyya, G.B. Viswanathan, R. Denkenberger, D. Furrer, H.L. Fraser, The role of crystallographic and geometrical relationships between  $\alpha$  and  $\beta$  phases in an  $\alpha/\beta$  titanium alloy, *Acta Mater.* 51 (2003) 4679–4691.
- [39] T. Kurzynowski, K. Gruber, W. Stopyra, B. Kuźnicka, E. Chlebus, Correlation between process parameters, microstructure and properties of 316L stainless steel processed by selective laser melting, *Mater. Sci. Eng., A* 718 (2018) 64–73.
- [40] W. Kurz, D.J. Fisher, *Fundamentals of Solidification*, third ed., Trans Tech Publications Ltd, 1986.



- [41] S.A. David, J.M. Vitek, Correlation between solidification parameters and weld microstructures, *Int. Mater. Rev.* 34 (5) (1989) 213–244.
- [42] J.L. Murray, The Ti–V (Titanium–Vanadium) system, in: *Bulletin of Alloy Phase Diagrams*, vol. 2, ASM, 1981, pp. 48–55.
- [43] J.C. Schuster, J. Palm, Reassessment of the binary aluminum–titanium phase diagram, *Phase Equilib. Diffus.* 27 (3) (2006) 255–277.
- [44] Y. Mishini, C. Herzig, Diffusion in the Ti–Al system, *Acta Mater.* 48 (2000) 589–623.
- [45] H. Nakajima, S. Ohshida, K. Nonaka, Y. Yoshida, Diffusion of iron in  $\beta$  Ti–Fe alloys, *Scripta Mater.* 34 (6) (1996) 949–953.
- [46] J.F. Murdock, C.J. McHarguet, Self-diffusion in body-centred cubic titanium–vanadium alloys, *Acta Metall.* 16 (1968) 493–500.
- [47] T. Takahashi, Y. Minamino, M. Komatsu, Interdiffusion in  $\beta$  phase of the ternary Ti–Al–V system, *Mater. Trans. Japan Inst. Metals* 49 (1) (2008) 125–132.
- [48] B. Baufeld, O. Van der Biest, R. Gault, Additive manufacturing of Ti–6Al–4V components by shaped metal deposition: microstructure and mechanical properties, *Mater. Des.* 31 (2010) S106–S111.
- [49] S. Mishra, T. DebRoy, Measurements and Monte Carlo simulation of grain growth in the heat-affected zone of Ti–6Al–4V welds, *Acta Mater.* 52 (2004) 1183–1192.
- [50] B. Radhakrishnan, S. Gorti, S.S. Babu, Phase field simulations of autocatalytic formation of alpha lamellar colonies in Ti–6Al–4V, *Metall. Mater. Trans.* 47 (2016) 6577–6592.
- [51] I. Katzarov, S. Malinov, W. Sha, Metall. Finite element modeling of the morphology of  $\beta$  to  $\alpha$  Phase transformation in Ti–6Al–4V Alloy, *Mater. Trans.* 33A (2002) 1027–1040.
- [52] M. Neikter, P. Åkerfeldt, R. Pederson, M.-L. Antti, V. Sandell, Microstructural characterization and comparison of Ti–6Al–4V manufactured with different additive manufacturing processes, *Mater. Char.* 143 (2018) 68–75.